Spinodal decomposition in 3-space

Aritomo Shinozaki* and Yoshitsugu Oono
Department of Physics, Materials Research Laboratory and Beckman Institute, University of Illinois at Urbana-Champaign, 1110 West Green, Urbana, Illinois 61801-3080
(Received 22 February 1993)

Using a cell-dynamical system (CDS) to model the separation of phases, we present the results of large-scale simulations of spinodal decomposition in 3-space of a symmetric binary alloy and incompressible binary fluid at critical quench. Our main results are (1) the reliable determination of the asymptotic or the almost asymptotic form factors for these systems, and (2) an understanding of the preasymptotic behavior of growth laws in terms of dispersion relations of interface fluctuations. To achieve (1) it is indispensable to have (i) methods to analyze the data, (ii) a scheme to simulate a system with fluid dynamic interactions, and (iii) a demonstration of the self-averaging nature of spherically averaged quantities. Item (iii) allows us to study sufficiently large systems with currently available computational resources. A careful stability analysis of our CDS model (such as artificial pinning, anisotropy, etc.) is also given. We must point out that the conventional data analysis coupled with artificial pinning and finite-size effects may spuriously give the theoretically desired results, especially in binary fluids. The asymptotic form factors are estimated in collage form from our large-scale late-time simulation results and various theoretical asymptotic results such as Tomita's sum rule. We may conclude that for binary fluids, the agreement between our form factor and ones obtained experimentally is excellent. This also clearly demonstrates that apart from time- and space-scale changes binary polymer systems so far studied and low-molecular-weight systems are not distinct; that is, no polymer effect has been observed in the form factor. In the case of binary alloys, the agreement with our form factor and various experimental results is not as good as the binary fluid case. This may be ascribed to various complications in solids, anisotropy, elastic effects, etc.

PACS number(s): 64.75.+g, 64.70.Kb, 61.20.Ja

I. INTRODUCTION

A full understanding of the nature of spinodal decomposition, the growth of domains of two stable phases from an initial homogeneous unstable state, has been the focus of much theoretical, experimental and computational study. Unfortunately, no complete theory of the late stages is available for even the simplest model of spinodal decomposition, i.e., the Cahn-Hilliard (CH) [1] equation, and no sufficiently large-scale three-dimensional (3D) computational study has been available, especially for binary fluids. We believe that reliable computational results would facilitate constructing better analytical approaches to the problem.

In the present paper, we give large-scale and late-time computational results of the cell-dynamics system (CDS) [2,3] description of spinodal decomposition in symmetric binary-alloy and binary-fluid systems. Our ultimate goal is to estimate the truly asymptotic form factors and to understand the differences between the systems with and without fluid dynamic effects. To this end, we introduce ways to analyze data, a scheme to simulate systems with fluid dynamics, and a way to understand preasymptotic results. We also critically assess the reliability of the CDS.

We will be concerned with the late stages of spinodal decomposition where scaling is postulated to occur [4,5]. This implies that $S(q,t)=l^d F(ql(t))$, where $l(t)$ is the representative scale of the coarsening patterns at time t and F is a master scaling function. An alternative to ordinary scaling is multiscaling [6]: $S(q,t)\propto l(t)^{\phi(ql(t))}$, where $\phi(x)$ is a universal function. From the results of a previous paper [7], we do not believe that multiscaling occurs in the CH-equation-type phase separation dynamics. In the presence of scaling, we expect that the growth law for $l(t)$ obeys a power law, $l(t)\sim t^{\alpha}$, asymptotically in time. If one assumes that there is a unique length scale governing the spatial patterns at each instant, then dimensional analysis gives us the exponents of the growth law depending on the dynamics [8,9]. For binary alloy systems modeled by a CH-type equation, one expects $\alpha=\frac{1}{3}$ (see also [10,11]). For binary-fluid systems, quenched into a regime where there are interconnected domains, one expects $\alpha=1$. Many experiments have demonstrated scaling and power-law growth for systems as diverse as binary alloys [12–15], quasibinary glasses [16], simple fluids [17,18], and polymeric fluids [19,20].

Numerical studies of spinodal decomposition have been primarily carried out by Monte Carlo methods, molecular dynamics, nonlinear (Langevin) equations, or CDS. Monte Carlo simulations of the Ising model using Kawasaki spin-exchange dynamics have been done for 2D [21,22] and 3D [23] systems. Although it is difficult to generate large data sets and long-time simulation, numerical renormalization-group techniques have been employed to support scaling and a late-time exponent of $\frac{1}{3}$ [22]. A finite-size scaling approach has also been used to support a $\frac{1}{3}$ growth exponent [24]. Realistic fluid dynam-

ics using the Monte Carlo technique does not appear feasible. Molecular dynamics can simulate only a small system for a short time [25], which is insufficient to produce detailed data on the form factor or correlation function. Another method is to solve directly nonlinear models such as the CH equation [26,27]. However, to attain late-stage behavior, large time steps are necessary. This leads directly to the consideration of *a priori* discrete space-time models called cell-dynamical systems (CDS's). Such mesoscale models have been used to study spinodal decomposition in realistic systems: 2D [28,29] and 3D [30] systems, 2D binary fluid in a Hele-Shaw cell [31], and 3D incompressible binary fluid [32]. These studies generally support scaling, at least within their respective types of dynamics, and more closely approach the asymptotic exponents derived by dimensional analysis than do direct Monte Carlo simulations.

Even with the aid of a computationally efficient CDS, unambiguously studying the late-stage asymptotic behavior is not a very easy task due to limitations in computational speed or memory. Therefore, it is important to have some definitive asymptotic theoretical results in order to guide and test the computational studies. For CH-type spinodal decomposition, it has been demonstrated that $S(q,t)\sim q^4$ for small q [33,34]. For binary-fluid decomposition, this has not been motivated theoretically, but experiments seem to support the exponent 4 as a lower bound. For large q, Tomita [35] has derived general expressions for the form factor which are generalizations of Porod's law, i.e., $S(q)\sim q^{-d+1}$. Tomita also derived a sum rule which is useful for checking the asymptoticity of the form factors.

In Sec. II, we first summarize the phenomenological and asymptotic results which we use to analyze our data. Next, we explain the methods used to analyze our numerical data, form factors, and growth laws. We point out that the conventionally defined average wave number $\langle k \rangle$ may give grossly misleading results, especially in the case of binary fluids. In Sec. III, CDS models are introduced. We explain the concept "qualitative accuracy" [3], and demonstrate that the CDS spinodal model can be understood as a qualitatively accurate discretization of the CH equation. Alternatively, the CH equation is a qualitatively accurate partial differential equation describing the CDS model. We use a split scheme to efficiently calculate spinodal decomposition in binary fluids.

In Sec. IV, we present a preliminary computational study of "damage spreading" in 3-space spinodal decomposition for both ordinary and fluid systems. The range of damage grows only as fast as the coarsening length scale $l(t)$. Rescaling the damage spreading envelopes by the coarsening length scale shows that they are bounded by a fixed exponentially decaying envelope. This result suggests that perturbing the initial conditions of a subsystem of a larger system affects other subsystems only within a range comparable to the length scale $l(t)$. Hence, subsystems lying beyond this range should be statistically independent. This, in turn, implies that shell-averaged quantities such as the spherically averaged scattering form factor or correlation function do self-average. Thus a few samples of a large system simulation can give very accurate results. This is a key observation for effectively using limited computational resources.

In Sec. V, we exhibit scaling of the form factors of our symmetric alloy and fluid system. Using a hardening procedure on the decomposition pattern [30], we demonstrate that a universal form factor can be obtained from preasymptotic data. With the aid of the known asymptotic theoretical results, we construct a collage of the functional form of the form factors and correlation functions for both alloy and fluid cases. For the fluid system, we are also able to exhibit the full velocity-velocity correlation function over time. This function has a scaling structure and appears to obey k^{-6} for $k \gg 1$, which may be interpreted as $k^{-(n+d)}$ due to Bray and Puri [36], and Toyoki [37].

In Sec. VI, we discuss the growth law. Since it is impossible to get the true asymptotic growth law by means of any computational approach, we must somehow extrapolate the computational results into the asymptotic regime. To this end, it is very important to understand the preasymptotic behavior of the length scale $l(t)$. We demonstrate that the dispersion relation around the kink solution [38–40] is a key to understanding the preasymptotic growth law in both alloy and fluid cases. The result strongly suggests that in contrast to binary alloys, we cannot ignore the contribution from the essential spectrum for binary fluids.

Section VII summarizes our finding.

II. PRELIMINARIES

A. Phenomenology

In this paper we study the systems described by a scalar order parameter $\psi(\mathbf{r},t)$, where $\mathbf{r}$ denotes the position. The order parameter is an appropriately normalized concentration difference of the two components. The real-space correlation function is $G(\mathbf{r},t)\equiv\langle\psi(\mathbf{r},t)\psi(0,t)\rangle$, where $\langle\ \rangle$ denotes ensemble averaging. The form factor $S(\mathbf{k},t)$ is its Fourier transform. Assuming isotropy, we define $S(k,t)$ and $G(r,t)$ as the spherically averaged form factor and correlation function [t may often be suppressed as $S(k)$ and $G(r)$]. In the late stages, the domain pattern formed by the segregated phases at a given time is conjectured to be statistically similar to the pattern at a later time [4,5,41]. This implies that $S(k)$ should be determined by a master form factor, $F(Q)=l(t)^{-3}S(k,t)$, where $Q=kl(t)$ with a single time-dependent length scale $l(t)$. This also applies to the correlation function as $G(\rho)=G(r,t)$, where $\rho=r/l(t)$.

A few theories describe the asymptotic properties that the scattering form factor should obey. The most basic is Porod's law [42] which states that $\lim_{k\to\infty}k^{d+1}S(k)=C_d A$ in d-space, where $C_3=2\pi$, and A is the area density of the interfaces. This follows from the assumption that random interfaces are smooth and thin. In conjunction with Porod's law, there is the Tomita sum rule [43] for $S(q)$: $\int_0^\infty[k^{d+1}S(k)-C_d A]=0$. This result should hold for any phase ordering system in the limit that the interfacial width is small with respect to the pattern size.

The counterpart to Porod's law and the Tomita sum rule for the real-space correlation function is $\lim_{r\to 0}[\nabla^2 G(r)+B_d A/r]=0$ and, assuming isotropy, $G(r)=G(0)-B_d ArE(r)$, where $E(r)$ is an even function of r and $B_3=\frac{1}{2}$.

Using more information about the principal curvatures on the interfacial surface, Tomita [35] extracted the next order behavior of $G(r)$ and $S(k)$. Defining $R_i(a)$ as the ith principal curvature, where a is the coordinate on the interface, and $i\in\{1,2,\ldots,d-1\}$, there is an invariant

$$\bar{R}_m^{-2}=\frac{\int d^{d-1}a\left[2\sum_{j=1}^{d-1}R_j^{-2}(a)+\left[\sum_{j=1}^{d-1}R_j^{-1}(a)\right]^2\right]}{\int d^{d-1}a}. \tag{1}$$

Tomita found, for small r,

$$G(r)=G(0)-B_d Ar\left[1-(d-1)\frac{r^2}{24\bar{R}_m^2}+\cdots\right] \tag{2}$$

and, for large k,

$$S(k)=C_d Ak^{-(d+1)}\left[1+\frac{(d^2-1)}{8\bar{R}_m^2}k^{-2}+\cdots\right]. \tag{3}$$

For small k, Yeung [33] reasoned from the CH equation that $S(k)\sim k^{\delta}$, where $\delta\geq 4$ asymptotically, if scaling and $l(t)\sim t^{1/3}$ holds. It has been postulated that this is exactly $S(k)\sim k^4$ if the chemical potential behaves globally as a random variable [34]. This is made more explicit by Tomita [44], who demonstrated that the k^2 term in $S(k)$ would vanish if the system is isotropic and chemical potential has no long-range correlation.

B. Data analysis

Numerically, we use a discrete Fourier transform defined by

$$\psi_{\mathbf{k}}(t)=\sum_{\mathbf{n}}\exp(i\mathbf{k}\cdot\mathbf{n})\psi(\mathbf{n},t),$$
$$\psi(\mathbf{n},t)=\frac{1}{N^d}\sum_{\mathbf{k}}\psi_{\mathbf{k}}(t)\exp(-i\mathbf{k}\cdot\mathbf{n}), \tag{4}$$

where $\mathbf{k}=2\pi\mathbf{n}/N$, $\mathbf{n}\in\{0,1,\ldots,N-1\}^d$, and N is the linear lattice dimension. We invariably impose periodic boundary conditions in this paper. Numerically, $S(\mathbf{k},t)=\langle\psi_{-\mathbf{k}}(t)\psi_{\mathbf{k}}(t)\rangle$ is easier to obtain, where the average is over the ensemble of systems studied. The correlation function is given by $G(\mathbf{n},t)=N^{-d}\sum_{\mathbf{k}}\exp(-i\mathbf{k}\cdot\mathbf{n})S(\mathbf{k},t)$.

The scattering function and correlation function are usually represented in a spherically averaged form. This is defined by applying a shell averaging procedure,

$$S(k)=\frac{1}{N_k}\sum_{\mathbf{k}'\in\Delta(k)}S(\mathbf{k}'), \tag{5}$$

where N_k is the number of points in the shell in k-space $\Delta(k)\equiv\{\mathbf{k}'\mid k-\frac{1}{2}\Delta<|\mathbf{k}'|<k+\frac{1}{2}\Delta\}$, with Δ being the width of the shell. The points k are taken at regular intervals starting at zero. The spherically averaged correlation function $G(r)$ $(r=|\mathbf{n}|)$ is generated analogously to the above. The bin averaging described here for $S(k)$ for $\Delta=2\pi/N$ skews the weight of data points in $S(\mathbf{k})$, especially when $\Delta(k)$ contains only a few vectors. For example, let us choose $k=2\pi/N$ and $\Delta=2\pi/N$. Then in 2-space, the shell contains four vectors with $|\mathbf{k}|=2\pi/N$ and four with $|\mathbf{k}|=\sqrt{2}(2\pi/N)$. Although the bin is defined as centered at $k=2\pi/N$, the average value of k in the shell is $\sim 1.2(2\pi/N)$. In this paper, we will plot $S(k)$ versus $k_w(k)$, where $k_w(k)$ is the average of $|\mathbf{k}|$ in the k shell, i.e.,

$$k_w(k)=\frac{1}{N_k}\sum_{\mathbf{k}'\in\Delta(k)}|\mathbf{k}'|. \tag{6}$$

This adjustment greatly improves the scaling of $S(k)$ for smaller k when $\langle k\rangle$ is small. This is important, because at late times, $S(k)$ is represented by very few points about the peak, all at small k.

Traditionally, one defines the characteristic length scale of the pattern size based on $G(r)$ or $S(k)$. The first zero crossing of $G(r)$ is one such scale. The inverse of $\langle k\rangle$,

$$\langle k\rangle\equiv\int dk\,kS(k)\Big/\int dk\,S(k), \tag{7}$$

is another. The average $\langle k\rangle$, defined by (7), depends on the discrete integration of $S(k)$, which may have very few points near its peak. This leads empirically to a drastic systematic error in $\langle k\rangle$. For example, in Fig. 1, we generate a simple curve as a test form factor, $F(Q)=Q^4/(1+Q^8)$. The scattering function is $S(k)\propto F(k/\langle k\rangle)$, and we sample it at discrete k as if it were the spherically averaged $S(k)$ for a system of size $N=64$. Using this, we generate a computed $\langle k\rangle$ according to (7) and compare this with the actual $\langle k\rangle$ (see Fig. 2). We note that at small $\langle k\rangle$, the measure can significantly overestimate the change of $\langle k\rangle$. The effective growth exponent is defined by

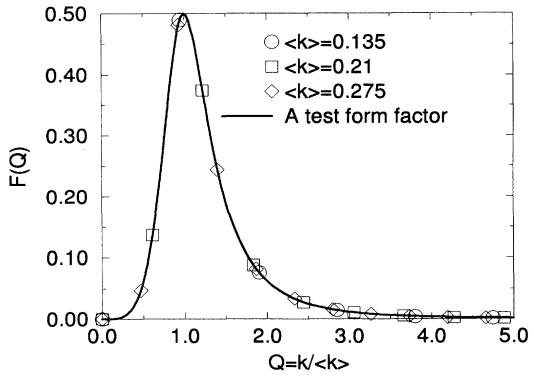

FIG. 1. Test form factor $F(Q)=Q^4/(1+Q^8)$ used to generate a mock measurement of $\langle k\rangle$ from discrete $S(k)$. Points shown are discrete points of $S(k)$ for $\langle k\rangle=0.135$, 0.21, and 0.275; the linear system size is assumed to be $N=64$.

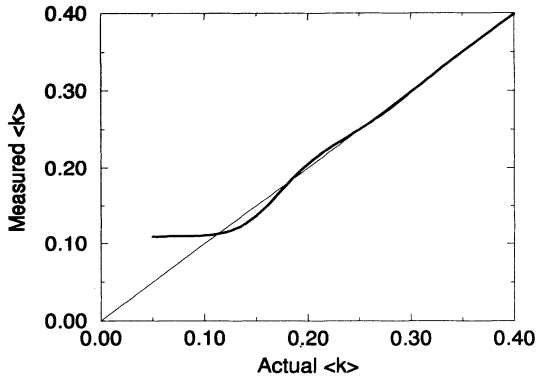

FIG. 2. Plot of $\langle k \rangle$ defined by (7) vs true $\langle k \rangle$. The linear system size is assumed to be $N=64$, and the measured form factor is simply the discretely sampled points of an actual exact test form factor in (1).

$\alpha \equiv -\partial \ln(\langle k \rangle)/\partial \ln(t)$. Suppose that $\langle k \rangle \propto t^{-1/3}$, then the exponent should be uniformly $\frac{1}{3}$. With the above systematic errors occurring as in Fig. 3, there could be serious misinterpretation of the asymptotic exponent, depending on at which $\langle k \rangle$ the data was terminated.

We find that a new $\langle k \rangle$ defined by

$$\langle k \rangle \equiv \frac{\sum_{\mathbf{k}\neq\mathbf{0}} |\mathbf{k}|^{-1} S(\mathbf{k})}{\sum_{\mathbf{k}\neq\mathbf{0}} |\mathbf{k}|^{-2} S(\mathbf{k})} \tag{8}$$

eliminates this systematic error, and is consistent with the old $\langle k \rangle$ when there are sufficient number of points in $S(k)$. Figure 4 demonstrates the behavior of the old and new $\langle k \rangle$'s on the actual data of simulations with different system sizes. We note that the new $\langle k \rangle$ follows the old $\langle k \rangle$ until the systematic error begins. Further, the new $\langle k \rangle$ of a small system smoothly follows the $\langle k \rangle$ applied to a larger system until very near the end of the growth of the smaller system's domains. In contrast, the old $\langle k \rangle$ has a distinct systematic error before the end of the growth. Note that the effect of the systematic error is to boost the effective exponent for small systems, bringing it much closer to the expected value of -1 than is actually indicated by the larger system.

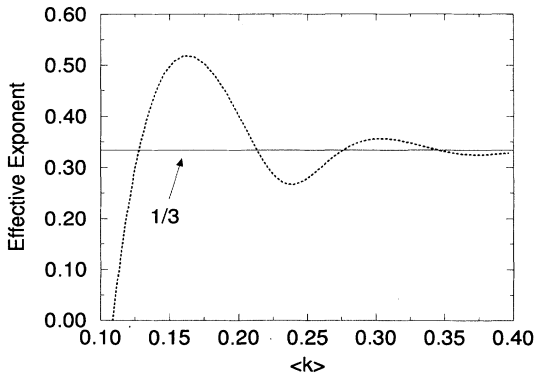

FIG. 3. Computation of the effective exponent assuming that the true law is of the form $\langle k \rangle = ct^{-1/3}$. Note that if linear regression were used from $\langle k \rangle = 0.4$ to 0.175, one might estimate the growth exponent to be significantly larger than $\frac{1}{3}$. This implies that even if the empirical exponent is less than $\frac{1}{3}$, one could erroneously conclude that the observed exponent is $\frac{1}{3}$.

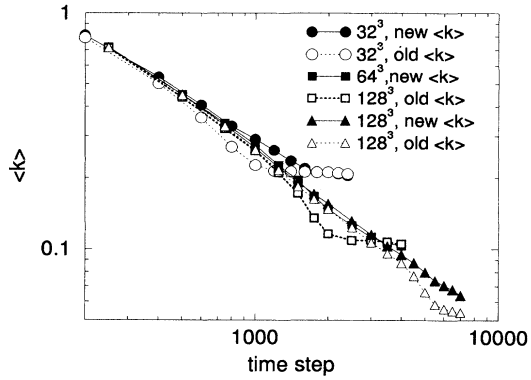

FIG. 4. Plot of $\langle k \rangle$ vs the time step of various-sized simulations of the binary-fluid decomposition. Solid points use a new measure of $\langle k \rangle$ (8), while unfilled points use the old measure (7). Note the systematic error induced by the old measure. For example, the 32^3 system measured by the old $\langle k \rangle$ would indicate a near $\langle k \rangle = t^{-1}$ growth law due to the systematic error. Model parameters are $M=1$, $D=0.7$, $\eta=1$, and $A=1.3$ with the tanh map.

III. CELL-DYNAMICAL MODELS

A. Model for spinodal decomposition

Spinodal decomposition is a typical nonlinear nonequilibrium phenomenon. Such phenomena are usually modeled in terms of partial differential equations (PDE) with nonlinear terms, and their analytic study is of limited use. Numerically solving them is indispensable, and space-time discretization is mandatory. Therefore, the most natural idea is to *ab initio* construct space-time discrete models to describe phenomena at the mesoscopic level. Such models would be preadapted to our computational means. We can even merge the modeling of the system and the devising of a numerical algorithms in this way. Thus we model space-time phenomena in terms of a map from a pattern at time t on a lattice L, $\{\psi_t(n)\}_{n\in L}$, to that at time $t+1$, $\{\psi_{t+1}(n)\}_{n\in L}$, where $\psi_t(n)$ is a quantity at the nth lattice point at time t. The quantity can be a scalar, tensor, or even a picture, so we imagine these quantities to live in a cell attached to each lattice point. We call such systems cell-dynamical systems (CDS's) [2,3]. The essence of the *ab initio* construction of a CDS model of a phenomenon is to model mesoscopic scale fluctuations directly in terms of the dynamics of each cell and relations among them.

The important features of the mesoscopic fluctuations of a system undergoing spinodal decomposition are (1) the local tendency to segregate (tendency to increase the local concentration difference), (2) the stability of the segregated bulk phases, and (3) the conservation of matter. A convenient variable to describe the

configuration of a binary mixture is the concentration difference ψ of the two components, normalized between -1 and 1. The simplest model incorporating all these features reads [28]

$$\psi_{t+1}(\mathbf{n})=\psi_t(\mathbf{n})+M[I_t(\mathbf{n})-\langle\langle I_t(\mathbf{n})\rangle\rangle] , \tag{9}$$

$$I_t(\mathbf{n})=D[\langle\langle \psi_t(\mathbf{n})\rangle\rangle-\psi_t(\mathbf{n})]+\mathcal{F}(\psi_t(\mathbf{n}))-\psi_t(\mathbf{n}) . \tag{10}$$

Here $\mathcal{F}(\ )$ defines a symmetric hyperbolic map with one source at the origin and two sinks. $\langle\langle\ \rangle\rangle$ is a suitable isotropic neighborhood average (see Sec. III C) and D is a positive numerical constant describing the stability of the bulk uniformity. I_t is the increment of ψ if there is no conservation constraint, and can be interpreted as $I_t \propto -\mu$, where μ is the effective chemical potential. M is a mobility constant. We will refer to the discrete time steps in the CDS modeling as t_{CDS}. For mesoscale phase separation, noise has been found to be irrelevant [45].

Strictly speaking, we need not worry about the relation of our CDS model to PDE models, the CH equation in our case:

$$\frac{\partial\psi}{\partial t}=-M\Delta(D\Delta\psi+\tau\psi-g\psi^3) , \tag{11}$$

where M, D, τ, and g are positive phenomenological constants. The CH equation is a phenomenological model just as the CDS model, so there is no particular reason to favor the PDE model over the CDS model or vice versa. Our original claim [10] was that the mathematical essence of spinodal decomposition is beyond the distinction of discrete and continuous models. Because we do not have any suitable language to describe this mathematical structure, we use PDE or CDS reluctantly. Hence it is important that both capture the structure. We now give a supporting argument to the assertion that they both capture the same physics.

The overall Laplacian in the CH equation imposes the conservation law, so we pay attention to the nonconserved counterpart which is a semilinear parabolic equation of the following form

$$\frac{\partial\psi}{\partial t}=D\Delta\psi+g(\psi) . \tag{12}$$

Let us introduce the solution semigroup $\mathcal{F}_s$ of the corresponding ordinary differential equation

$$\frac{d\mathcal{F}_s(\psi_t)}{ds}=g(\mathcal{F}_s(\psi_t)) . \tag{13}$$

The formal solution of (12) is given by

$$\psi_{t+\delta t}(x)=\int dy\, G(x-y,\delta t)\psi_t(y) + \int_0^{\delta t} ds \int dy\, G(x-y,\delta t-s)g(\psi_{t+s}(y)) , \tag{14}$$

where $G(x,t)$ is a fundamental solution for $\partial_t-D\Delta$ (recall the principle of "not feeling the boundary"). Use (13) as an approximate local solution to (12) for short times, and integrate (14) by parts to get

$$\begin{aligned}\psi_{t+\delta t}(x)&\approx\int dy\, G(x-y,\delta t)\psi_t(y)+\int_0^{\delta t} ds\int dy\, G(x-y,\delta t-s)\frac{d\mathcal{F}_s(\psi_t(y))}{ds} ,\\ &=\mathcal{F}_{\delta t}(\psi_t(x))+D\Delta\int_0^{\delta t} ds\int dy\, G(x-y,\delta t-s)\mathcal{F}_s(\psi_t(y)) .\end{aligned} \tag{15}$$

If δt is sufficiently small, then $G(x-y,\delta t-s)\simeq\delta(x-y)$, so (15) reduces to the semigroup discretization proposed in [28] as the crudest approximation to (15). Imposing the conservation law and choosing the unit of time to be δt, we get (10). Changing δt corresponds to changing the map $\mathcal{F}_{\delta t}$. But the map is always symmetric around the origin which is a hyperbolic source, and there are two hyperbolic sinks irrespective of δt. At least empirically, we know that the asymptotic form factor and the time dependence are independent of the choice of the map (universality), and of the choice of the isotropized averaging operator. Notice that for sufficiently small δt and fine spatial discretization, the CDS models reduce to the simple Euler scheme. With the aid of this universality, we conclude that the Euler scheme for sufficiently small δt and the semigroup scheme for reasonably large δt give the same asymptotic behavior. In other words, the CDS model and the CH equation give identical asymptotic macroscopic results.

It should be emphasized that although the above argument allows us to regard the CDS model as a discretization scheme of the CH equation in a certain sense, the CDS model is not a PDE solver in any standard sense of numerical analysis. Obviously, the solution obtained by the CDS equation with a large δt and a large spatial increment cannot give any accurate solution to the initial value problem of the CH equation. Still, the macroscopic observables are quantitatively accurate. This implies that a new concept, the *qualitative accuracy,* of numerical analysis is possible [3]. We say a scheme is qualitatively accurate if the scheme can give quantitatively accurate results about the quantities which qualitatively characterize the system. Thus we claim that when seen as a discretization scheme the CDS spinodal model is a qualitatively accurate discretization method for the CH equation. Of course, we can also say that the CH equation is a qualitatively accurate continuum counterpart of the CDS spinodal decomposition model. The relation between the "diffusion constants" D in both models will be mentioned in Sec. III C. This qualitative accuracy is possible because the mathematical structure governing the late-stage spinodal decomposition allows both discrete and continuum modeling. The reason for this seems to be a sort of renormalization-group structure, but we have

not been able to exploit this analytically. Qualitative accuracy is a blessing, since the CH equation has never been solved numerically as a PDE for sufficiently long time. The coarse discretization scheme utilized to solve the CH equation only solved an inefficient CDS model.

If Kawasaki exchange dynamics is honestly modeled, then the CDS spinodal model must be modified. One such model proposed in [46], which corresponds to the PDE model proposed by Langer [47], and by Kitahara and Imada [48], is

$$\frac{\partial\psi}{\partial t}=-\nabla\cdot(1-a\psi^2)\nabla(D\Delta\psi+\tau\psi-g\psi^3)\ , \tag{16}$$

where a is a positive constant not larger than $\sqrt{g/\tau}$. Extensive numerical study of this equation has been performed [49]. The modification becomes significant if gravity cannot be ignored or if the quench is extremely deep, but otherwise it is not believed to be so crucial. In this paper, we do not adopt this modification. Kawasaki exchange is an artificial dynamics for Monte Carlo simulations, and it is naive to believe that the Monte Carlo models are more realistic than the above phenomenological model. The same criticism applies to lattice-gas approaches as well.

B. Model with hydrodynamics interactions

A basic PDE model that embodies the essential physics of the slow incompressible flow of a binary mixture driven by the gradients of the chemical potential is given in [9]. Typically, one considers a coarse grained free energy $F_{\rm CG}$ which may have the typical Landau-Ginzburg form. The associated chemical potential gradient, $\nabla\mu=\nabla(\delta F_{\rm CG}/\delta\psi)$ drives a diffusive current, i.e., the ordinary CH dynamics, and provides a driving force on the incompressible binary fluid. Under the assumptions that the fluid velocity $\mathbf{v}$ is slow and slaved to the phase separation dynamics, and that the (kinematic) viscosity η is independent of ψ, one may make the approximation:

$$\Delta\mathbf{v}=\frac{1}{\eta}(\nabla p-\psi\nabla\mu)\ , \tag{17}$$

with the incompressibility constraint $\nabla\cdot\mathbf{v}=0$. Combining this with the CH equation, one arrives at the following closed equations first derived by Kawasaki [50]:

$$\frac{\partial\psi}{\partial t}=M\Delta\frac{\delta F}{\delta\psi}-[\nabla\psi(r)]\int\mathcal{T}(r-r')[\nabla'\psi(r')]\frac{\delta F}{\delta\psi}(r')\ , \tag{18}$$

where $\mathcal{T}$ is the Oseen tensor. One could proceed by naively discretizing this equation. However, the resulting discrete model would be difficult to simulate due to the small time steps required for a stable simulation. Further, the convolution integral requires $O(N^{2d})$ steps, where N is the linear system size.

As our starting point, we use a CDS model of spinodal decomposition of a symmetric binary alloy. This provides us a computational model for the ordinary part of the dynamics. Then the fluid flow is computed using fast-Fourier-transform (FFT) techniques. One could model the effect of fluid flow as has been done in our Hele-Shaw model [31,51] or later in Koga and Kawasaki [32] by faithfully adding the fluid flow into the update of the order parameter. We will call this model the additive model. While this is in the spirit of the original equation (18), we found empirically that such a model could be significantly unstable for large time steps or small viscosity. The dissipative part of the dynamics primarily maintains the shape of the domain walls and stabilizes the bulk. The hydrodynamic flow part advects large domains. At large time steps, the hydrodynamic flow, implemented on a discrete lattice, has a distorting effect on the shape of the walls and on the bulk. In the additive model, the result of the dissipative term is added directly to the distorted result of the advection. In the next time step, the fluid flow reacts via the driving force to the now distorted pattern, leading to further distortion. This situation is further exacerbated by the fact that the modes which stabilize the bulk can be slower than the hydrodynamic modes which move the domain walls [40]. This is discussed further in Sec. VI B.

We avoid this difficulty by the following approach. Writing equation (18) symbolically as

$$\frac{\partial\psi}{\partial t}=\mathcal{N}_{\rm CH}\psi+\mathcal{N}_H\psi\ , \tag{19}$$

where $\mathcal{N}_{\rm CH}$ is the nonlinear operator describing the conventional CH equation, and $\mathcal{N}_H$ the rest due to hydrodynamics. The formal solution is given in terms of the semigroup $\exp[\int dt(\mathcal{N}_{\rm CH}+\mathcal{N}_H)]$ (in terms of the time-ordered exponential). Approximating the integral as a Riemann sum, we can formally write

$$\exp\left[\int dt(\mathcal{N}_{\rm CH}+\mathcal{N}_H)\right]=\prod\exp[\Delta t\mathcal{N}_{\rm CH}]\exp[\Delta t\mathcal{N}_H]\ , \tag{20}$$

where we have used the idea of Trotter's formula. The discrepancy of both sides is of order Δt. This implies that updating for small Δt can be split into two operations, one describing the hydrodynamic advection effect, and the other describing the ordinary spinodal decomposition without hydrodynamics. Explicitly, this gives us in discretized time steps,

$$\psi_t^*=\psi_t-\Delta t\nabla\psi_t(r)\int\mathcal{T}(r-r')\nabla'\psi_t(r')\frac{\delta F}{\delta\psi}(\psi_t(r'))\ , \tag{21}$$

$$\psi_{t+\Delta t}=\psi_t^*+\Delta tM\Delta\frac{\delta F}{\delta\psi}(\psi_t^*)\ . \tag{22}$$

To further accelerate the simulation, we note that the spinodal pattern evolves slowly with time, so that the corresponding flow field also evolves slowly. The spinodal pattern usually shifts on the order of $\frac{1}{100}$ of a lattice space per time step during a typical simulation. Even if the actual fluid field were updated every ten time steps, it would reflect the fluid field of a pattern to within $\frac{1}{10}$ of a lattice space, which is still well below our course graining length scale.

We organize the numerical problem as follows. We

first compute the velocity field for this order-parameter field as

$$\mathbf{v}_t = \mathfrak{F}^{-1}\{\mathcal{T}_{\mathbf{k}}\mathfrak{F}[(-[\nabla]_c)\psi I_t]\}\ , \tag{23}$$

with

$$I_t = D[\langle\langle \psi_t \rangle\rangle - \psi_t] + \mathcal{F}(\psi_t) - \psi_t\ , \tag{24}$$

where $[\nabla]_c$ is the center difference discrete gradient operator, $\mathfrak{F}$ is the discrete FFT, and $\mathcal{T}_{\mathbf{k}}$ is the discrete version of the Fourier-transformed Oseen tensor constructed by solving (17) with a periodic boundary condition

$$\mathcal{T}_{\mathbf{k}} = \mathfrak{F}\left[\frac{1}{\eta}[\Delta]_c^{-1}\left[1+\frac{[\nabla]_c \otimes [\nabla]_c}{[\Delta]_c^{-1}}\right]\right]\ . \tag{25}$$

Here $[\Delta]_c^{-1}$ is inverse of the standard nearest-neighbor discrete Laplacian, and $[\nabla]_c$ is the center difference gradient. This discrete Oseen tensor is an approximation to the exact operator and is not an exact discrete projection operator to produce a divergenceless field. This is due to the incompatibility of the definition of $[\nabla]_c$ and $[\Delta]_c$ since $[\nabla]_c[\nabla]_c \neq [\Delta]_c$. The order-parameter field is then advected as

$$\psi_t^* = \psi_t - [\nabla]_c \cdot (\mathbf{v}_t \psi_t)\ . \tag{26}$$

In this way, the order parameter is still conserved under advection. Finally, we execute the ordinary dynamics on ψ_t^* to get ψ_{t+1}.

As noted above, since the velocity field does not usually change appreciably, we again execute the ordinary dynamics but use the velocity field without updating. This cycle is repeated a fixed number $n_{v\text{skip}}$ of times; we find empirically that $n_{v\text{skip}}=10$ was suitable for the parameters we are using. If we note a buildup of order parameter, we reduce $n_{v\text{skip}}$: $n_{v\text{skip}}=5$ if $\psi_{\max}>1.07$, 2 if $\psi_{\max}>1.075$, and 1 if $\psi_{\max}>1.08$. In the Appendix, we test this scheme (split scheme) versus the ordinary additive scheme with $n_{v\text{skip}}=1$. We note here that, mesoscopically, this scheme generates the same pattern, as measured by the form factor.

The velocity field update is about as CPU expensive as 10–20 ordinary dynamics time steps for a system of size 192^3. If we were to do a velocity field update each time step, the overall program would be prohibitively expensive to run on large systems. With the above, we are able to run several large systems at about 3–4 times the cost of the nonfluid dynamics system. Much of the time, the system ran at maximum $n_{v\text{skip}}$ with no problems. Empirically the value of $n_{v\text{skip}}$ succeeded in detecting situations where the field was rapidly reorganizing locally and avoided instability mentioned above.

Polymer systems undergoing spinodal decomposition have been extensively studied experimentally [19,52–54,20]. It is tempting to model the polymer system with a modification of the free-energy functional F in (17). de Gennes [55], Pincus [56], and Binder [57] also considered possible modifications of the kinetic coefficient. In principle, there are at least three relevant length scales in the problem: the pattern size $l(t)$, the polymer radius of gyration R_G, and the correlation length which is equal to interface thickness ξ. To describe spinodal decomposition kinetics, the system must be described at the subcorrelation length scale. Thus we cannot use the random-phase approximation at the scale of R_G as already pointed out in conjunction to the block copolymer segregation problem [51]. The Flory-Huggins-de Gennes (FHdG) free energy used in existing studies has the same difficulty. Furthermore, we do not know how realistic the reptation mechanism is in the melt. Thus no reliable theoretical or computational studies of the polymer effects on spinodal decomposition are possible.

The three representative length scales mentioned above are independent, at least in the scaling regime. But, as seen in [19,52], R_G and ξ appear to be proportional in actual experimental examples. Thus we may conclude that there has been no really deep quench symmetric spinodal experiment in polymers with fluid dynamics [58]. This strongly suggests that we do not need any special model to understand polymer spinodal decomposition in the regimes that have been accessed by real experiments. Our results indeed agree well with the results obtained by, e.g., Hashimoto and co-workers [19] as seen in Sec. V D. Actually, experimental results from polymeric systems are thus far the best quality for spinodal decomposition with fluid dynamical interactions. One might counter that there are polymer effects on spinodal decomposition, pointing out the so-called "N-branching" phenomenon [59], pattern freezing observed in the off-critical quenches [60], etc. Off-critical freezing occurs because one component cannot diffuse through the bulk phase of the other. Thus this is a true polymer effect, but the effect can reasonably be described by (16). Notice that the breaking of one phase into small domains itself due to off-criticality does not cause freezing, if the system is described by the CH equation with the free energy functional replaced by the FHdG form. The so-called "N-branching" phenomenon may be a much more interesting effect than off-critical freezing, but we believe that this can be accounted for by appropriate choice of parameters in the model. The nonuniversality in the preasymptotic growth law is, as discussed in Sec. VI B, not a genuine polymer effect. To observe more interesting polymer effects, we need a system which we can quench deeply. This means that one must mix rather incompatible polymers A and B to prepare the initial condition; simply raising the temperature is usually not enough. One possible way may be to use a mixture of A, B, and AB diblock copolymers. A more drastic means may be to use AB-diblock copolymers and break the AB covalent bond by irradiation, for example.

C. Pinning and instability

Before proceeding, we will consider various problems that may occur in heavily coarse-grained, discrete systems. Some of these problems have been addressed before [26,28], particularly the linear stability of uniform solutions and the occurrence of a slowing down of the system due to over coarse graining.

1. Pinning

In a previous study of spinodal decomposition of a binary fluid in a Hele-Shaw cell [31], we found for particular parameters that the domain walls of the system appeared to become gradually pinned to the underlying lattice structure of the simulation. This also exhibited itself as a slowing down of the expected growth law over time until the system froze. This pinning occurred for parameters that were deemed safe empirically from observation of the ordinary model of spinodal decomposition. This was ascribed to the ability of fluid flow to more efficiently rearrange the domain structure and to find the favorable pinned structures. Notice that the acceleration in development of the conventionally analyzed $\langle k \rangle$ due to finite-size effects countered with this pinning effect could give a false signal of the expected growth behavior $\langle k \rangle \propto t^{-1}$ for some intermediate time range.

To show the effect of pinning for the ordinary spinodal decomposition model, we make a trial 2D run. The neighborhood average is

$$\langle\langle \psi \rangle\rangle = \tfrac{1}{6} \sum_{\{\mathrm{NN}\}} \psi + \tfrac{1}{12} \sum_{\{\mathrm{NNN}\}} \psi \ , \tag{27}$$

where {NN} and {NNN} stand for nearest neighbor and next-nearest neighbor. The map is

$$\mathcal{F}(\psi) = A \tanh[\tanh^{-1}(1/A)\psi] \ , \tag{28}$$

which we call the tanh map, with $A = 1.5$. We varied D. The growth law is plotted in Fig. 5 over time for various D. Note that for $D \geq 0.067$, the growth of the system appears as the expected power law, while for $D < 0.067$ we find that the system slows down. Examination of the spatial pattern finds that the walls pin to the underlying lattice. Note that D used here is related to the D_{CDS} in 2-space by $D = (\frac{1}{3}) D_{\mathrm{CDS}}$ and in 3-space by $D = (\frac{11}{40}) D_{\mathrm{CDS}}$. Such relations will be discussed briefly in Sec. III C.

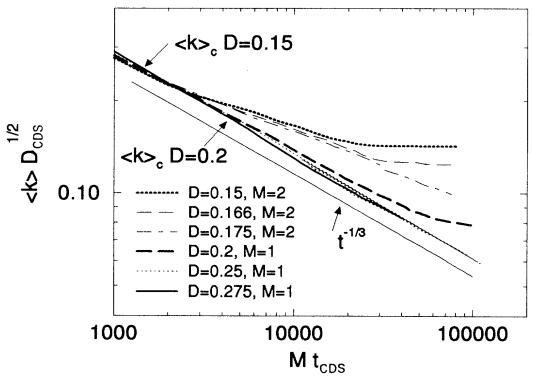

FIG. 5. Plot of $\langle k \rangle$ for the 2D spinodal decomposition model with various D_{CDS}. The plot is scaled by plotting $\langle k \rangle D_{\mathrm{CDS}}^{1/2}$ vs $t_{\mathrm{CDS}} M$. For $D_{\mathrm{CDS}} = 0.15$–0.175, pinning is obvious as $\langle k \rangle$ starts to slow down significantly from the expected $t^{-1/3}$ law. $D_{\mathrm{CDS}} = 0.25$ and higher appear to be unaffected. $D_{\mathrm{CDS}} = 0.2$ appears almost normal until very late in the run. Data are taken from a single 128^2 sample run. For $D_{\mathrm{CDS}} = 0.15$ and 0.2, arrows mark $\langle k \rangle_c$ where the pinning effect is estimated to start. A reference line for $t^{-1/3}$ is also plotted.

To assess the numerical pinning, we examine the equilibrium solution to the discrete flat interfacial wall:

$$-D[\Delta]_c \psi + \mu_0(\psi) = 0 \ , \tag{29}$$

where $\mu_0 = \mathcal{F}(\psi) - \psi$ and $[\Delta]_c$ is the usual three-point discrete Laplacian, $\psi_{i+1} + \psi_{i-1} - 2\psi_i$. We solve this numerically on a unit discrete 1D lattice with coordinate n, with $\psi(n)$ describing the order parameter. The boundary conditions are $\psi(-N/2) = -\psi_{\mathrm{bulk}}$ and $\psi(N/2) = \psi_{\mathrm{bulk}}$. We solve this with two special conditions: $\psi(0) = 0$ ("the zero condition") and $-\psi(0) = \psi(1)$ ("the center condition"). We note that the discrete free energy which generates Eq. (29) as a first-order variation is the usual

$$\sum_n [\tfrac{1}{2} D \{[\nabla]_n \psi(n)\}^2 + f(\psi(n))] \ , \tag{30}$$

where $f(\psi) = \int_{\psi_0}^{\psi} [\mathcal{F}(\psi) - \psi] d\psi$, and $[\nabla]_n \psi(i) = \psi(i+1) - \psi(i)$. In Fig. 6, we graph, for various D, $\Delta\sigma = \sigma_{\mathrm{zero}} - \sigma_{\mathrm{center}}$ using the tanh map with $A = 1.5$, where the discrete surface free energy (σ) for the zero and center equilibrium solutions are denoted as σ_{zero} and σ_{center}, respectively. We note that the freezing appears for $\sigma_{\mathrm{zero}}/\sigma_{\mathrm{center}} > 1.14$ for this system size.

Consider a section of the interface with mean curvature K. The driving force due to curvature is $f_{\mathrm{curv}} = (d-1)\sigma K$. The force due to the pinning effect is roughly $f_{\mathrm{pin}} = \Delta\sigma$ [(lattice space)/2]$^{-1}$. From this we get a criterion that the lattice pinning effect will compete with the curvature driven dynamics when

$$\frac{\Delta\sigma}{\sigma} \sim \frac{d-1}{2} K \ . \tag{31}$$

Estimating that $K = 4\lambda^{-1}$ with $\langle k \rangle \lambda = 2\pi$, we find that the $\langle k \rangle_c$, where pinning effect may become important, is

$$\langle k \rangle_c = \frac{\pi}{d-1} \frac{\Delta\sigma}{\sigma} \ . \tag{32}$$

For example, for the above 2D model, with $D_{\mathrm{CDS}}^{\mathrm{2D}} = 0.15$, 0.175, and 0.2, we find $\langle k \rangle_c = 0.65$, 0.57, and 0.43, respectively. The first two estimates correspond to the $\langle k \rangle$ where we do see the effects of the pinning in Fig. 5. For

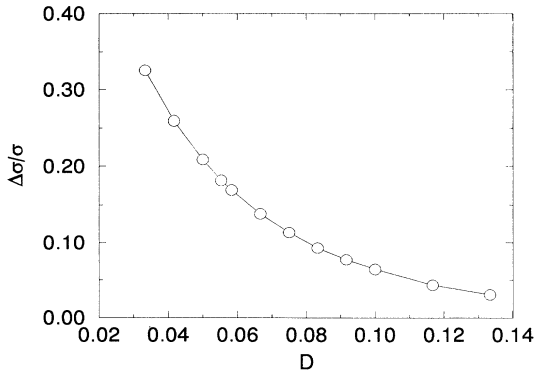

FIG. 6. The ratio $\Delta\sigma/\sigma$, as determined numerically, is plotted against D. Note that D here is related to D_{CDS} by $D = \frac{1}{3} D_{\mathrm{CDS}}$ in 2D and $D = \frac{11}{40} D_{\mathrm{CDS}}$ in 3D.

$D_{\rm CDS}^{\rm 2D}=0.2$ we do not see any discernible pinning effect until very late. However, in the Hele-Shaw system, for $A=1.5$, $D_{\rm CDS}^{\rm 2D}=0.2$, we did see pinning occur, starting at about $\langle k\rangle\sim 0.32$. Thus we can see how $\Delta\sigma/\sigma$ contributes to numerical pinning. It is important to note that even when pinning should take place, its effect seems to grow smaller as $\Delta\sigma/\sigma$ gets smaller. Thus the ordinary 2D system does not appear to be affected at the estimated $\langle k\rangle_c$ for $\Delta\sigma/\sigma\sim 0.12$. Thus we feel it is safe to proceed as long as $\Delta\sigma/\sigma<0.1$. For our later work, we generally run with $\Delta\sigma/\sigma<0.07$, and in the case of the hydrodynamic model we have $\Delta\sigma/\sigma=0.03$.

2. Discrete Laplacian

We define the discrete Fourier transform as (4). The usual discrete Laplacian (times $1/2d$) in 3-space is

$$f(\mathbf{x})\equiv\tfrac{1}{6}[\Delta]_c\psi(\mathbf{x})=\tfrac{1}{6}\sum_{\mathbf{x}'\in \mathrm{NN}(x)}\psi(\mathbf{x}')-\psi(\mathbf{x})\ , \tag{33}$$

where $\mathrm{NN}(x)$ stands for nearest neighbors to $\mathbf{x}$. The Fourier transform of the above yields

$$F(\mathbf{k})=\{\tfrac{1}{3}[\cos(k_1)+\cos(k_2)+\cos(k_3)-\tfrac{1}{2}]\}\psi_{\mathbf{k}}\ . \tag{34}$$

We use a 3D neighborhood average defined as

$$\langle\langle\psi\rangle\rangle=\tfrac{6}{80}\sum_{\{\mathrm{NN}\}}\psi+\tfrac{3}{80}\sum_{\{\mathrm{NNN}\}}\psi+\tfrac{1}{80}\sum_{\{\mathrm{NNNN}\}}\psi\ , \tag{35}$$

where $\{\mathrm{NNNN}\}$ stands for next-next-nearest neighbor. For $f(x)=\langle\langle\psi\rangle\rangle-\psi$, we get

$$\begin{aligned}F(\mathbf{k})=\{&\tfrac{6}{80}[2\cos(2\pi k_x)+2\cos(2\pi k_y)+2\cos(2\pi k_z)]\\&+\tfrac{3}{80}[4\cos(2\pi k_x)\cos(2\pi k_y)+4\cos(2\pi k_x)\cos(2\pi k_z)+4\cos(2\pi k_y)\cos(2\pi k_z)]\ ,\\&+\tfrac{8}{80}\cos(2\pi k_x)\cos(2\pi k_y)\cos(2\pi k_z)-1\}\psi_{\mathbf{k}}\ .\end{aligned} \tag{36}$$

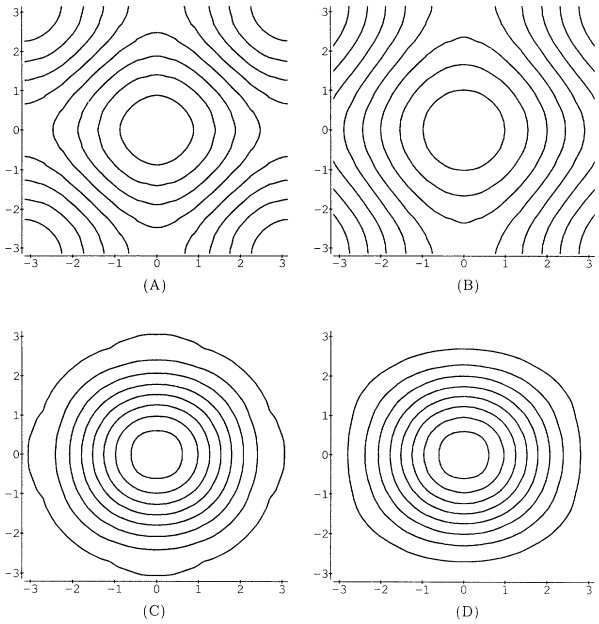

FIG. 7. (A) Plot of isocontour lines of the usual discrete Fourier-transformed Laplacian looking down the [001] axis. (B) Isocontour lines of the usual discrete Laplacian looking down the [011] axis. (C) 6:3:1 "Laplacian" looking down the [001] axis. (D) 6:3:1 "Laplacian" looking down the [011] axis.

In Fig. 7, it is clear that this more complex 6:3:1 "Laplacian" has the desirable property of being more generally isotropic, especially at small to medium scales. A better form is possible, but for our purpose this is enough. This type of analysis has been done for the 2D counterpart by Tomita [44], who showed that Eq. (27) is optimal.

In Eq. (11), constants D and M are roughly related to D and M in the CDS models by looking at the small-k behavior along an axis. In this paper, we will generally use $D_{\rm CDS}$ or $M_{\rm CDS}$ for the CDS model coefficients unless otherwise clear from context. The relation between the coefficients depends on the dimension and averaging used. For the averaging used above, in 2-space, $D=\frac{1}{3}D_{\rm CDS}$ and, in 3-space, $D=\frac{11}{40}D_{\rm CDS}$, where Δt is chosen to be the unit time.

3. Bulk instability

We check the condition for linear stability of the CDS model. Recalling Eq. (10), we may easily linearize the equations about a constant $\psi=\psi_0$, and Fourier transform to get

$$\begin{aligned}\psi_{\mathbf{k}}^{t+1}&=\psi_{\mathbf{k}}^{t}-M_{\rm CDS}L_{\mathbf{k}}I_{\mathbf{k}}^{t}\ ,\\ I_{\mathbf{k}}^{t}&=\mathcal{F}'(\psi_0)\psi_{\mathbf{k}}^{t}+D_{\rm CDS}L_{\mathbf{k}}\psi_{\mathbf{k}}^{t}-\psi_{\mathbf{k}}^{t}\ ,\end{aligned} \tag{37}$$

where $L_{\mathbf{k}}$ is the Fourier transform of the operator $\langle\langle\cdots\rangle\rangle-\cdots$ and $\mathcal{F}'$ is the derivative of the map $\mathcal{F}(\psi)$. We may rewrite the above as

$$\psi_{\mathbf{k}}^{t+1}=H_{\mathbf{k}}(\psi_0)\psi_{\mathbf{k}}^{t}\ , \tag{38}$$

where

$$H_{\mathbf{k}}(\psi_0)=1-M_{\rm CDS}L_{\mathbf{k}}[\mathcal{F}'(\psi_0)+D_{\rm CDS}L_{\mathbf{k}}-1]\ . \tag{39}$$

For the bulk $\psi=\psi_{\rm bulk}$ to be stable, we want $|H_{\mathbf{k}}(\psi_{\rm bulk})|<1$, for $k\neq 0$.

$H_{\mathbf{k}}$ is plotted in Fig. 8 along an axis, for $\psi_0=0$ and for $\psi_0=\pm 1$, using the Laplacian defined by Eq. (36), and the tanh map with $A=1.15$, $D_{\rm CDS}=0.7$ and $A=1.3$, $D_{\rm CDS}=0.7$. At small scales, we see that $H_{\mathbf{k}}$ may take on

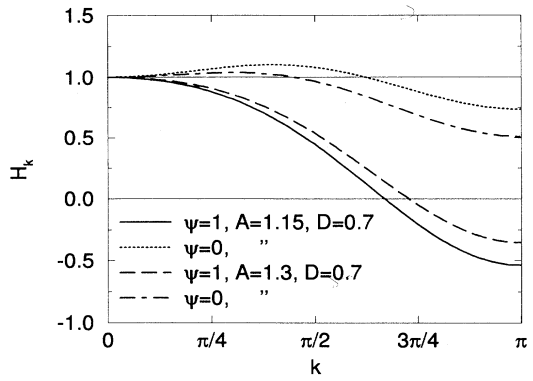

FIG. 8. Plot of H_k for $\psi=1$ and 0 appropriate to the CDS model using the map $\mathcal{F}(\psi)=A\tanh[\tanh^{-1}(A^{-1})\psi]$. For two different sets of parameters, $A=1.15$, $D=0.7$, and $A=1.3$, $D=0.7$.

negative values. As long as $|H_{\mathbf{k}}|<1$, the high wave-vector behavior, especially for $|k|>2$, of the bulk should be of no consequence. At $\psi=0$ we see the instability leading to the initial phase separation where $H_{\mathbf{k}}>1$. The structure of wave vector $|k|>2$ is suppressed from the initial conditions, and thus plays little role in the structure of the spinodal decomposition.

D. Computational costs

For the spinodal decomposition model without hydrodynamics, the cost on a Hewlett-Packard model 9000/730 was about 15.9 s per time step for a 128^3 system. On a Convex C-3840 (four processors), each time step took 3 s for a 128^3 system. On a Cray-2, a 192^3 system took 1 s per time step. In each case, one uses an easily computed empirical approximation to the tanh function:

$$\tanh(x)\approx\frac{7.7}{\pi^2}p(x)[1+0.02p(x)^2]\times\left[\left[1+\frac{4}{\pi^2}p(x)^2\right]^{-1}+\left[3.3+\frac{4}{\pi^2}p(x)^2\right]^{-1}\right], \tag{40}$$

where $p(x)=x-0.025x^3$. This approximation is satisfactory for $|x|<3.5$. Such a detailed approximation is not at all necessary, but allows easier comparison with previous studies using the tanh function. The tanh map we use in the CDS models is computed so as to set the stable fixed points at $\psi=\pm1$. This is done by computing $F(\psi)=A\tanh(B\psi)$ where $B=\tanh^{-1}(1/A)$. When using the approximation of the tanh function, the fixed points are close to, but not exactly ±1.

For the binary-fluid model, with $n_{v\text{skip}}=10$, and without there being any adaptation, the Convex C-3 could process on average one time step every 7.3 s for a 128^3 system. The Cray-2 could process one time step every 8 s for a 192^3 system. When an adaptation in $n_{v\text{skip}}$ was needed, as in the main $\eta=1$ 192^3 simulations, the time per step could vary, but on average attained one time step every 22 s.

IV. AVERAGING AND DAMAGE SPREADING

A. Fluctuations in form factor

To get reliable results from simulations with unfortunately fairly severely limited resources, we must study the necessary number of samples and the system size carefully. Milchev, Binder, and Heermann [61] demonstrated that the statistical errors cannot be reduced with the aid of a large system size, because the form factor lacks the so-called self-averaging property. They recommended that if one has a fixed amount of resources, it is better to study numerous smaller systems rather than fewer larger systems. This recommendation has been followed almost unanimously. Thus Koga and Kawasaki [32] studied the 3D spinodal decomposition with hydrodynamics with the aid of numerous 64^3 systems.

Unfortunately, as we will demonstrate, such a small system is quite inappropriate to obtain the asymptotic properties of a system such as the form factor. The representative length scale must be more than ten times as large as the interface thickness of the system [62]. Furthermore, the system size should be at least a few times as large as the pattern size. Thus in the case of the ordinary spinodal decomposition, we need at least $3\times10\times(5-6)$ linear lattice size, where 3 is the smallest possible thickness of the interface to avoid pinning. But it is extremely difficult to study 100 samples of 200^3 systems.

Milchev, Binder, and Heermann's recommendation implies that, even in real experiments, to get a reliable form factor, one must study many samples. But of course this is not the case. A single large sample usually gives a beautiful form factor without large errors (we ignore the subtlety of subtracting the background, etc. in this discussion.) In this paper we do not follow the recommendation. Actually, we wish to recommend the opposite: Try to study as big a system as one can, reducing the number of samples considerably. In this section we explain the rationale behind this proposal. In essence, what is overlooked in Milchev, Binder, and Heermann's recommendation is the noise structure in the form factor. At each $\mathbf{k}$, Milchev, Binder, and Heermann are absolutely right to claim that the fluctuation is of the same order of the averaged quantity. But for large systems, these fluctuations in different but adjacent k's are fairly uncorrelated, so the local averaging of the form factor over k almost eliminates the fluctuations. There is a question as to the bin size required to average out the statistical errors. If the ratio L/L_I of the system size L and the size of the statistically independent volume L_I is small, then the bin size cannot be made small, but if the ratio is sufficiently large, a very small bin is enough to average out the fluctuations. This explains the real experimental results.

For simplicity, we consider a discrete lattice system whose order parameter is ψ, and define the empirical form factor

$$s(\mathbf{k})\equiv\frac{1}{N^2}\sum_{\mathbf{n},\mathbf{m}}\exp[i\mathbf{k}\cdot(\mathbf{n}-\mathbf{m})]\psi(\mathbf{n})\psi(\mathbf{m}), \tag{41}$$

where N is the total number of lattice points. The ensem-

ble average denoted by $\langle s(k)\rangle$ (i.e., the average over samples) is the form factor $S(k)$. To get a zeroth-order estimate of the fluctuation, we assume that ψ is a Gaussian stochastic field. This is not a correct assumption, but it is sufficiently realistic as we will see soon. We get

$$\langle s(\mathbf{k})^2\rangle-\langle s(\mathbf{k})\rangle^2=S(\mathbf{k})^2+S(\mathbf{k})^2\delta_{\mathbf{k},0}\ . \tag{42}$$

This is independent of the system size. Hence, as Milchev, Binder, and Heermann claimed, the large fluctuation of the empirical $s(\mathbf{k})$, which is illustrated in Fig. 9, cannot be reduced by increasing the system size, but only by increasing the number of independent samples. Figure 9 demonstrates that (42), a consequence of the Gaussian assumption, is reasonable for most k except around $k/\langle k\rangle\sim 1.3$ [63].

Next, let us write down the cross correlations of $s(\mathbf{k})$ with different $\mathbf{k}$ with the same Gaussian assumption:

$$\langle s(\mathbf{k})s(\mathbf{k}')\rangle-\langle s(\mathbf{k})\rangle\langle s(\mathbf{k}')\rangle$$
$$=S(\mathbf{k})S(\mathbf{k}')[\Delta(\mathbf{k}-\mathbf{k}')+\Delta(\mathbf{k}+\mathbf{k}')]\ , \tag{43}$$

where

$$\Delta(\mathbf{k})=\frac{1}{N^2}\left|\sum_{\mathbf{n}} e^{i\mathbf{n}\cdot\mathbf{k}}\right|^2\ . \tag{44}$$

Here Δ is the familiar interference factor, and is very small when $|\mathbf{k}-\mathbf{k}'|$ is nonzero (actually zero for inverse lattice vectors), and the moving average of $s(k)$ should almost eliminate the fluctuations from the empirical form factor.

However, if an extensive moving average is required to this end, the resolution of the obtained form factor would be poor. Note that the form factor does not change appreciably over $\Delta k\sim 1/L_I$. That is, we can average $s(k)$ over this interval without distorting the form factor. Equation (44) implies that if the difference of k and k' is of order $1/L$, then the fluctuations are statistically independent. Hence the ratio L/L_I must be the key factor. It is sensible to assume that L_I is of the order of the pattern size, but this will be checked explicitly soon below. The number of $s(k)$ in the bin of size Δk is $\sim\Delta k k^{d-1}L^d$, since the density of the k vector is L^d. Let $k\sim n/L$. Then the number of k vectors we can average without distorting the form factor is $\sim n^{d-1}L/L_I$. This implies that if $L/L_I\sim 10$, then we can reduce the fluctuation by the factor of at least ~ 3 even for a very small wave vector.

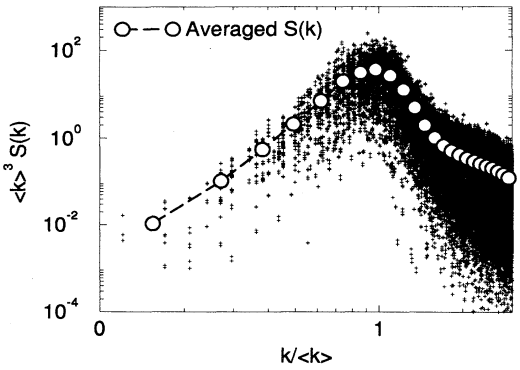

FIG. 9. Plot of $S(k)$ of a given sample done without averaging. Each plus represents $S(\mathbf{k})$ for some $\mathbf{k}$ where $k=|\mathbf{k}|$. This is plotted against the spherically and ensemble averaged $S(k)$. The fluctuation one sees in the single sample $S(k)$ does not change with system size, but the density of the points does.

A simple demonstration of this is to check the fluctuation of $S(k)$ versus system size. We do this by looking at $S(k)$ near the peak, using a bin of size $2\pi/N$, where N is the linear system size. For four 192^3 samples, with $\langle k\rangle\sim 0.2$, for a point $k/\langle k\rangle\sim 1$, we find that $\langle S(k)\rangle=28.8$, and that the standard deviation $\sigma=1.2$. There are 450 points in the shell for this bin. The Gaussian estimate is $\sigma=\langle S(k)\rangle/\sqrt{450}\approx 1.4$. For four 128^3 samples, with $\langle k\rangle\sim 0.2$, we find $\langle S(k)\rangle=27.7$, and $\sigma=2.6$. The Gaussian estimate is $\sigma=\langle S(k)\rangle/\sqrt{210}\approx 1.9$. For eight 64^3 samples, with $\langle k\rangle\sim 0.2$, we find $\langle S(k)\rangle=20.4$, and $\sigma=4.4$. The Gaussian estimate is $\sigma=\langle S(k)\rangle/\sqrt{62}\approx 2.6$. While the above is not a definitive study due to the small number of samples, it does indicate that the Gaussian estimate for the fluctuation of the spherically averaged quantities works well, and generally improves with larger system size. Also note that if we had chosen to fix the bin size in k space independent of system size, the fluctuation for larger sized systems would have decreased faster.

B. Damage spreading

The remaining task is to estimate L_I. We study this through the study of the propagation of disturbances in the initial conditions (essentially a damage-spreading study [64]). Since the study sheds further light on the dynamical nature of spinodal decomposition, here we give more details than required to estimate L_I. The damage-spreading experiment consists of looking at the difference of two samples which differ only by a small localized change of the initial conditions.

We ran two systems with almost identical random initial conditions distributed between ± 0.05. The only difference between the two systems was in a single cell of the initial random field. One sample had the cell set to $+0.05$ and the other sample had the cell set to -0.05. We then followed the evolution of the difference between the two samples. For this preliminary study, we took eight different random initial conditions and applied ordinary and hydrodynamic models to them. Each initial condition was studied with the damage described above. The samples were size 64^3 and we used the tanh map with parameters $A=1.3$ and $D=0.7$. The hydrodynamic model used a viscosity of $\eta=1.0$. Let ψ_1 be the order-parameter field of one sample and ψ_2 be that of the other sample.

As a global measure of the effect of the damage, we use the l^2 norm: $\|\psi_1-\psi_2\|_2\equiv\sqrt{\sum_{\mathbf{n}}(\psi_1(\mathbf{n})-\psi_2(\mathbf{n}))}$. To see the difference dynamics plays, we compute the l^2 norm of the damage over time for the ordinary and hydrodynamic models with identical parameters. This is shown in Fig. 10. As we can see, until $t_{\mathrm{CDS}}\sim 300$, the l^2 norm behaves

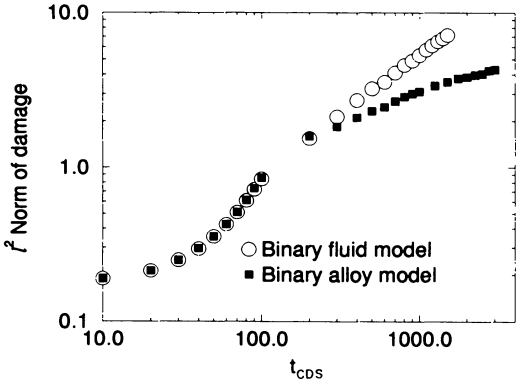

FIG. 10. Plot of the l^2 norm of the damage over time for binary-alloy and binary-fluid dynamics.

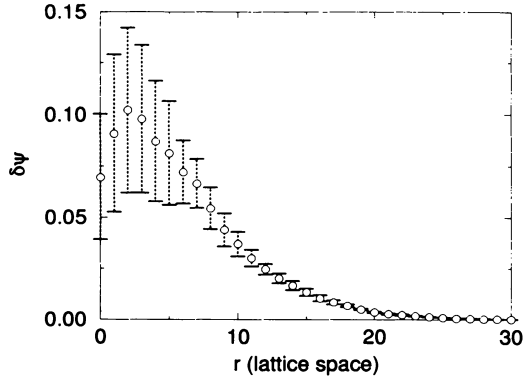

FIG. 12. Plot of the damage envelope and estimated error bars for time step 1000 of a binary-alloy dynamics simulation. There were eight samples of size 64^3 used.

identically. Beyond this time, the different dynamics causes the damage to spread differently. The l^2 norm of the damage for fluid systems grows nearly like t^1, while that for ordinary systems grows like $t^{1/3}$. This suggests that the damage spread scales with the characteristic length scale of the spinodal patterns. In Fig. 11 we see that the l^2 norm does appear to grow asymptotically like $\langle k \rangle^{-1}$. This strongly supports the assumption that there is only one representative length scale in the problem.

At a given time, we looked at $\delta\psi(\mathbf{r}) \equiv |\psi_1(\mathbf{r}) - \psi_2(\mathbf{r})|$, where the coordinate $\mathbf{r}$ is centered at the initial damage. The damage caused widely varying effects, depending on the initial condition, so the details of the envelope close to the center of damage may be obscure, but the tail of the envelope is well established (Fig. 12). We can superpose the damage envelopes at different but late times by plotting them versus $r\langle k \rangle$ (Figs. 13 and 14). Figure 15 compares the damage envelope of the binary-alloy and binary-fluid models at times when the two systems have the same global damage as determined by the l^2 norm. In either case, the damage envelope is at least exponentially bounded, and appears to scale with $\langle k \rangle^{-1}$. That is, the range of effect of local perturbation to distant subsystems spreads like the growth of the domains. The hydro-

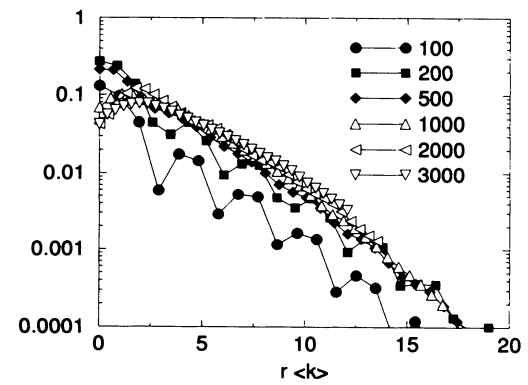

FIG. 13. Plot of the damage envelope for binary-alloy dynamics. The r axis is scaled by $\langle k \rangle$. Time steps 1000–3000 scale reasonably with a faster than exponential decay. In this figure and Fig. 14 the wavy form of the earliest time data indicates the concentric perturbation ripple running through the system due to the conservation law.

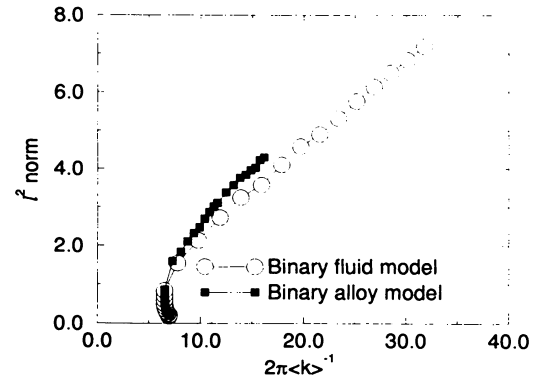

FIG. 11. Plot of the l^2 norm of the damage plotted against $\langle k \rangle$ of samples. The norm of the damage grows approximately linearly with $\langle k \rangle^{-1}$ asymptotically.

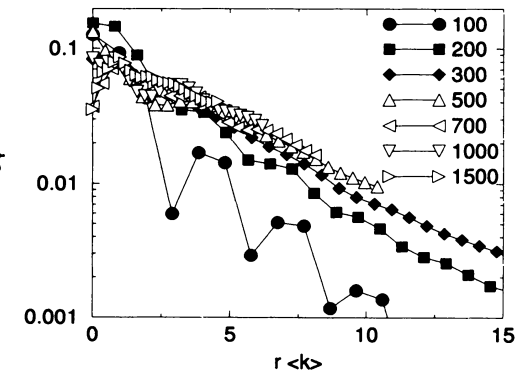

FIG. 14. Plot of the damage envelope for the binary fluid, removing any data from $r > 24$. Note that the maximum r is 32 for these simulations.

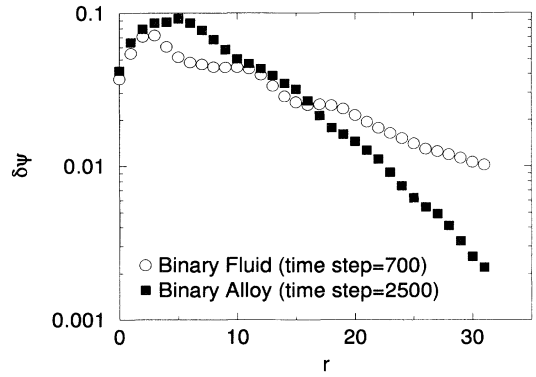

FIG. 15. Comparison between damage envelopes of binary-alloy and binary-fluid dynamics, compared when the l^2 norm of the damage is roughly the same. Note that the binary-fluid envelope is much shallower, but is still exponentially decaying.

dynamic model spreads out the damage more evenly than the ordinary system, with a generally lower amount of damage near the damage center, but with a tail that tapers off at a much slower exponential rate. This is consistent with the large-scale flow observed in binary-fluid systems.

Hence, beyond the average pattern size $\langle k \rangle^{-1}$, the lack of correlation due to the uncorrelated initial condition is maintained. We may conclude that there is statistical independence of subsystems of size $L_I > \langle k \rangle^{-1}(t)$. This is not as trivial as one might think; since a small point damage is like a small seed in a uniform unstable state, we see that concentric perturbation ripples run throughout the system, as can be seen from the earliest time data in Figs. 13 and 14.

V. CORRELATION FUNCTION AND FORM FACTORS

A. Binary alloy at critical quench

We will now describe our study of a symmetric binary alloy via the CDS spinodal model. A preliminary report has been published in [30]. In our study we have four 192^3 samples. The map we used was (28) with $A=1.15$ and $D=0.7$. The map that was actually used in the simulation was a simple approximation to the tanh map. Due to the nature of the approximate map the fixed point for the above A was $\psi_{\text{bulk}}=\pm 1.015$. Each sample was started from random initial conditions uniformly distributed in $[-0.05,+0.05]$. Each sample was run to $t_{\text{CDS}}=20\,000$ and periodically sampled to generate the spherically averaged scattering function and calculate $\langle k \rangle$ as explained in Sec. II B. Figure 16 shows a three-dimensional picture of the $\psi=0$ isosurface over various time steps.

In Fig. 17 we show the evolution of the probability density distribution of ψ for one sample over time. We note that at the latest time shown, the system has clearly separated into two distinct phases. At the earliest time shown, $t_{\text{CDS}}=1000$, the phases are not yet well segregated, and the peak of the distribution is not close to the bulk equilibrium value. However, as we will demonstrate in what follows, the asymptotic structure of the patterns is essentially set even at this early time.

In Fig. 18, we display the correlation function $G(r)$ over various times using a simple rescaling $G(\rho)\equiv G(r)$, where $\rho=r\langle k \rangle$. Away from the origin, $G(r)$ appears to approach a scaling form, as seen in Fig. 18. A better way to examine $G(\rho)$ is to look at $\rho^2 G(\rho)$, the integral of which is $\propto S(k=0)$. We note that $\rho^2 G(\rho)$ is more representative of the details of the system as perceived by the scattering function. In Fig. 19 it appears that the data are converging, at least in the region of $\rho<12$, to a universal form. Beyond $\rho>7$, the data from the latest time, $t_{\text{CDS}}=20\,000$, appear to deviate away from the other data. However, one must remember that at this time step, $\langle k \rangle \sim 0.25$, so that $\rho=20$ corresponds to $r=80$, which is roughly the limit on computing $G(r)$ due to the system size. In this instance, the conservation constraint and finite size of the system cause $r^2 G(r)$ to distort at large r.

We note that from the above observations that $G(r)$ does appear to be asymptotic of intermediate r at times before $G(0)\simeq 1$. If it were not for finite-size effects, one might suppose that scaling improves as r is larger. At small r, $G(r)$ is affected by the finite width of the inter-

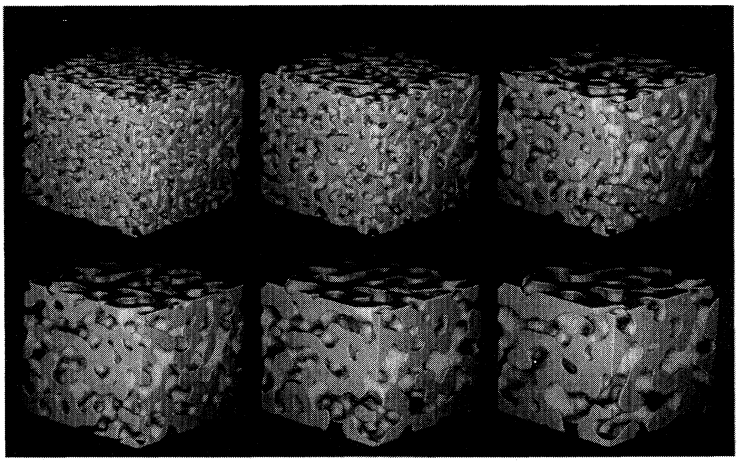

FIG. 16. $\psi=0$ isosurfaces of three-dimensional binary-alloy spinodal decomposition at critical quench. Parameters are $M_{\text{CDS}}=1$, $D_{\text{CDS}}=0.7$, and $A=1.15$ for the tanh map described in text. System size is 192^3. The images are a 128^3 subset of the entire sample. From top left to right, images are of $t_{\text{CDS}}=1000$, 2000, and 4000 data, and, from bottom left to right, of $t_{\text{CDS}}=7000$, 12 000, and 20 000 data.

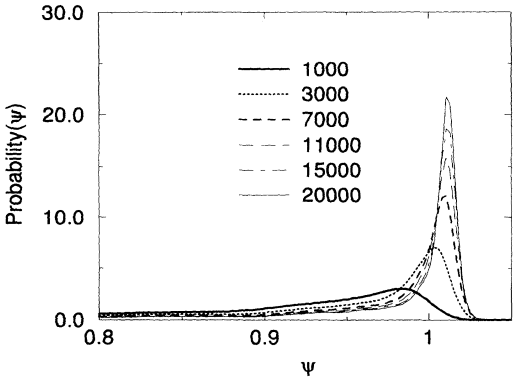

FIG. 17. Probability density distribution of ψ for the binary-alloy model, taken from a single 192^3 sample. Notice that for $t_{\mathrm{CDS}}=1000$ the distribution peak is well below the bulk equilibrium value of 1.015.

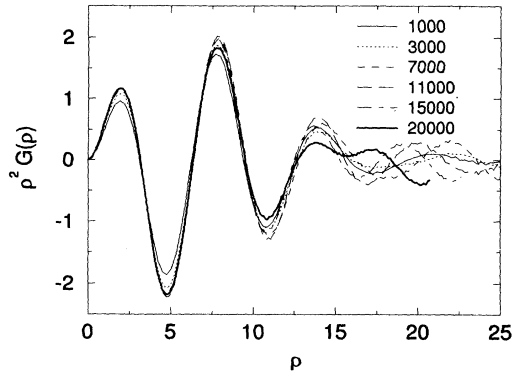

FIG. 19. Plot of $\rho^2 G(\rho)$ for the binary-alloy model. Note that the finite system size affects the tail of $G(\rho)$ at $t_{\mathrm{CDS}}=20\,000$ significantly. $\langle k\rangle\sim 0.2$ at this time step, thus $\rho=15$ corresponds to $r=75$, which is nearly half the system size.

face. Recall that $\psi^2_{\mathrm{bulk}}-G(0,t)\sim\xi\langle k\rangle$. If we can remove the influence of the finite interfacial width, scaling of $G(r)$ may be improved.

We conjecture a stronger version of the scaling hypothesis [30]: the physically relevant length scales that determine the form factor in the preasymptotic regime are the domain size and domain-wall thickness. Operationally, if we apply the transformation $\psi\rightarrow\mathrm{sgn}(\psi)$, the effect of the wall thickness on the correlation function will be removed. Data so processed will be called "hardened." If the stronger scaling hypothesis is correct, then the correlation function based on the hardened data should become time independent, and the resultant universal function can be interpreted as the asymptotic form. The hardening transformation can violate the conservation law, so that the form factor may not vanish at $k=0$ after hardening. However, the extent of the violation is extremely small at later times.

In Fig. 20, we see that the scaled $G(\rho)$ for hardened data does indeed become very nearly time independent over the same range of time as we showed in Fig. 18. If we look at $\rho^2 G(\rho)$ for the hardened data as in Fig. 21, we see that the data clearly collapse to a master form for a very wide range of $\rho=r\langle k\rangle$. Except for the latest time studied, $t_{\mathrm{CDS}}=20\,000$, all the data collapse over the range $0\le\rho\le 12$. If we are correct in interpreting the breakdown of $G(r)$ at large r as due to finite-size effects, we have confidence that our hardened data at $t_{\mathrm{CDS}}=1000$ may in fact give us a good look at asymptotic $G(\rho)$ for the range $0\le\rho\le 20$. Comparing $\rho^2 G(\rho)$ of the hardened data at $t_{\mathrm{CDS}}=1000$ and 3000 with the unhardened data at $t_{\mathrm{CDS}}=15\,000$, we note that the hardened data coincide for most of the graph with the regular data at $t_{\mathrm{CDS}}=15\,000$ up through $\rho\sim 15$. We recall from Fig. 17 that the data at $t_{\mathrm{CDS}}=1000$ is very clearly not well phase separated, and that the bulk of the domains is not yet well equilibrated. Thus it is remarkable that asymptotic features are actually present in the system.

Next we consider the scaled form factor, $F(Q)=\langle k\rangle^3 S(k)$, where $Q=k/\langle k\rangle$ for both regular and hardened data. Figure 22 shows the regular form factor. Scaling of the form factor is fair, with a small shift at later times. The reason for the continued evolution of the form factor is easy to see in the plot of $Q^4F(Q)$ or Porod's plot. Figure 23 shows that the large

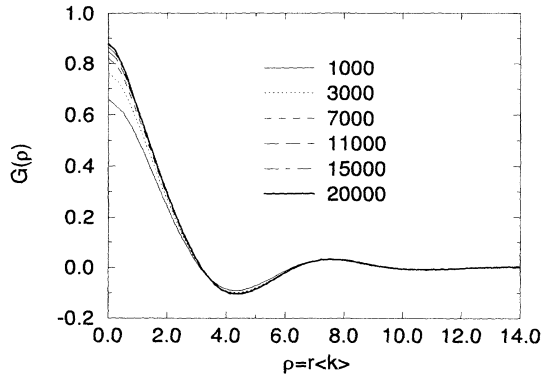

FIG. 18. Plot of the scaled correlation function $G(\rho)$ for the binary-alloy model. The peak of $G(\rho)$ is still 10% away from saturation at $t_{\mathrm{CDS}}=20\,000$.

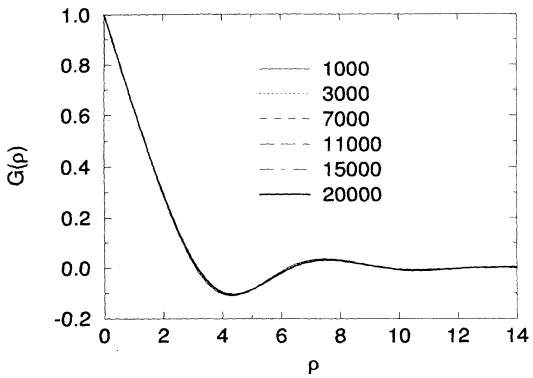

FIG. 20. Plot of $G(\rho)$ of hardened binary-alloy data. Note that the curves from each time step are nearly indistinguishable.

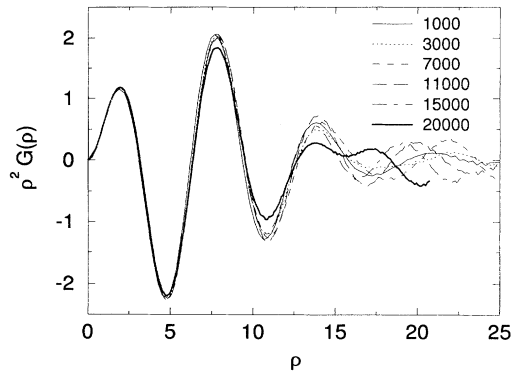

FIG. 21. Plot of $\rho^2 G(\rho)$ of hardened binary-alloy data. Even at this level, we have very good scaling up through $\rho=15$ for all time steps except 20 000. This is probably due to the finite size of the system coupled with conservation, which forces the $\rho^2 G(\rho)$ to be somewhat contorted.

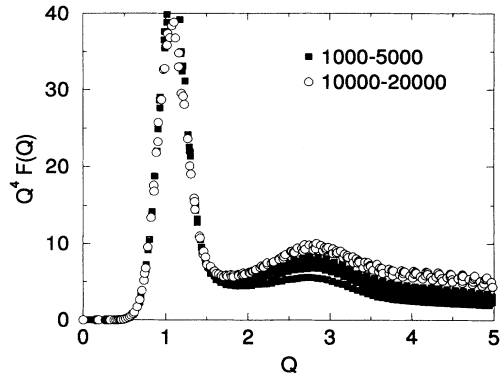

FIG. 23. Plot of $Q^4 F(Q)$ for the binary-alloy model. Dark filled circles are for combined $t_{\mathrm{CDS}}=1000-5000$ data. White filled circles are for time step combined 10 000–20 000 data. The tail continuously evolves upward over time. This evolution explains the slight shift in the form factor from early to late times. Due to the slow growth law, we cannot expect to see a Porod's tail in a reasonable computational time.

k tail of $Q^4 F(Q)$, for the regular data is continuing to rise with time. If one thinks of the preasymptotic pattern as being generated by mollifying the hardened pattern, for example by convoluting a Gaussian function, then the drooping tail is generated by the multiplication of $S(k)$ by $\exp(-\xi^2 k^2)$, where ξ is roughly the wall width. As the system coarsens, the exponential decay is fhited to higher and higher x since it is fixed in k. This would lead to a rising tail.

In Fig. 24, the scaling of the form factor of the hardened data is much better throughout the entire time range 1000–20 000. The difference in the form factor between the regular and hardened data is not very striking, but it is systematic. This difference is consistent with the shift in the form factor for the regular data between the early- and late-time data. In the Porod plot of the hardened data, Fig. 25, a clear time independence of the hardened $F(Q)$ for $0\leq Q\leq 4.0$ after $t_{\mathrm{CDS}}=5000$ is demon-

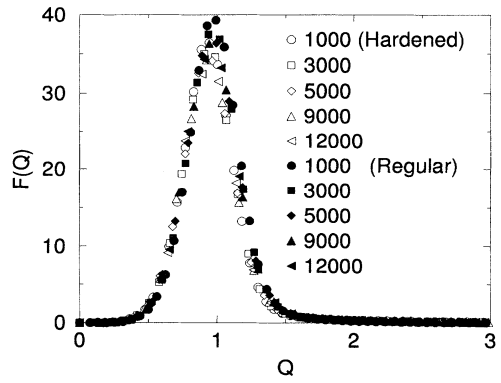

FIG. 24. Comparison plot of $F(Q)$ between regular and hardened data. The shift between the regular and hardened data is consistent with the shift we saw for early to late times in Fig. 22.

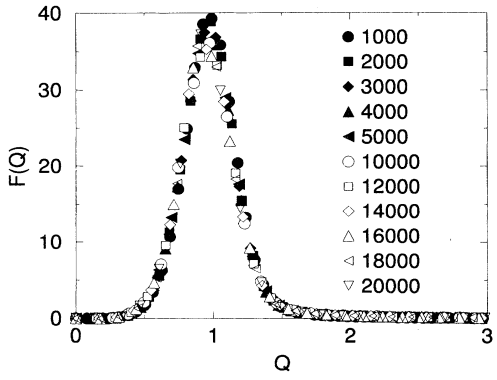

FIG. 22. Plot of $F(Q)\equiv\langle k\rangle^3 S(k)$ vs $Q\equiv k/\langle k\rangle$ over various time steps for the binary-alloy model. Black filled symbols are for early time data, time steps 1000–5000. White filled symbols are for late time data. Note that there is a shift in the form factor from early to late times.

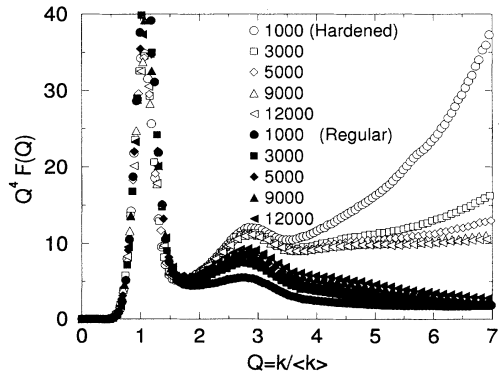

FIG. 25. Porod's plot $Q^4 F(Q)$ vs Q of both regular and hardened data. Note that the regular data high-k tail rise significantly throughout $Q>1.5$ while the hardened data converge toward a scaling form.

strated as stated in our previous paper [30]. Choosing the latest time available from the hardened data, we find that the Tomita sum rule holds very well with the asymptotic value of $Q^4F(Q)$ at $Q\sim 5$. The anomalous tail in the hardened Porod's plot is due to the discrete nature of the system. After hardening, the domain walls are very jagged. This jaggedness length scale shifts away in $F(Q)$ as $\langle k\rangle$ decreases, as we see at subsequent times in Fig. 25. Looking at both the regular and hardened data in Fig. 25, we see that there appears to be a convergence to a form between the hardened and regular data.

The extensive scaling of the hardened data demonstrates our stronger scaling hypothesis. Thus we feel that the hardened form factor does in fact represent the main features of the asymptotic form factor. The most notable feature of the Porod plot is the second peak located at about $k=2.9\langle k\rangle$. The Porod tail is due to the random, smoothly varying, infinitely thin interfacial wall. The first-order deviation is due to the local curvature. Hence the second hump represents a nontrivial set of curvature fluctuations, at a scale smaller than the main pattern size. It is also very likely that we have a third peak at around $k=5\langle k\rangle$.

Figure 26, the log-log plot of $F(Q)$ for the regular data, shows a very clear $F(Q)\sim Q^4$ behavior for small Q (Yeung's power law form). Interestingly, the Q^4 behavior appears to hold from about $Q=0.3$ or 0.4 on.

To extract the most self-consistent information for $G(r)$ and $S(k)$ from all the available data, we put together a collage of data, along with the asymptotic estimates for the small- and large-k behaviors of $S(k)$ and small-r behavior of $G(r)$. This is done in three parts.

(i) For small r and large k, Tomita generalized Porod's law to account for the curvature of the interfaces and found Eqs. (2) and (3). The hardened $S(k)$ data suffer at large k from the discrete nature of the patterns. However, $G(r)$ scales well at small r and allows us to fit the small-r behavior to the form of Eq. (2). To accomplish this, we look closely at the hardened $G(r)$. To see the small-r behavior best, we plot $E(\rho)=[1-G(\rho)]\rho^{-1}$ (Fig. 27). This should have the form of $E(\rho)=c_0-c_1\rho^2+c_2\rho^4-\cdots$. Several different time steps plotted in Fig. 27 exhibit a small but systematic evolution. To estimate the asymptotic values of c_0 and c_1, data from each time step are fit to the above form, and the obtained c_0 and c_1 are plotted versus $\langle k\rangle$ (Figs. 28 and 29). From this we estimate that $c_0=0.368$, and $c_1=0.0044$. We can measure A and $\bar{R}_m^2$ in units of $\langle k\rangle$ as $A=(4/\Delta\psi^2)c_0$ and $\bar{R}_m^2=c_0/(12c_1)$. We estimate that $A=0.368\langle k\rangle$, and $\bar{R}_m^2=7.0\langle k\rangle^{-2}$. In turn, this allows us to compute the large-x behavior of $F(Q)$ asymptotically. Plotting (3) versus the hardened data in Fig. 30, we see that the tail of $F(Q)$ matches extremely well for the latest times available from $Q>5$. Thus the Tomita form will be used for the tail of the collage $F(Q)$.

(ii) The slight nonconservation of the order parameter due to the hardening causes distortion of $F(Q)$ for small Q. For $0.8<Q<5$ the hardened form factors scale well. Hence, for intermediate Q consistent with the above tail

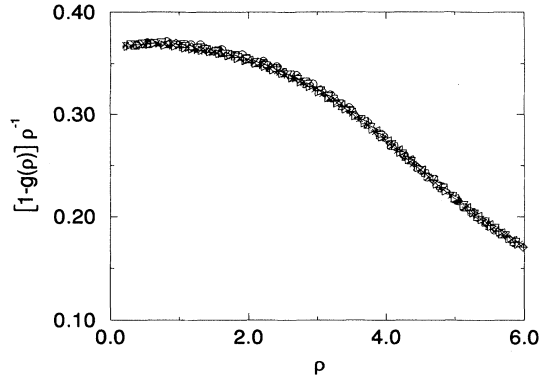

FIG. 27. Plot using hardened data of $[1-G(\rho)]\rho^{-1}$. Data from time steps 1000, 2000, 3000, 4000, 5000, 7000, 11 000, 15 000, and 20 000 are plotted. Scaling is very good, as expected. In general, the peak of the curves drops as the t_{CDS} increases, but it is not very noticeable here. Using this data, we may extract A, the area density of the interfaces, and $\bar{R}_m^2$.

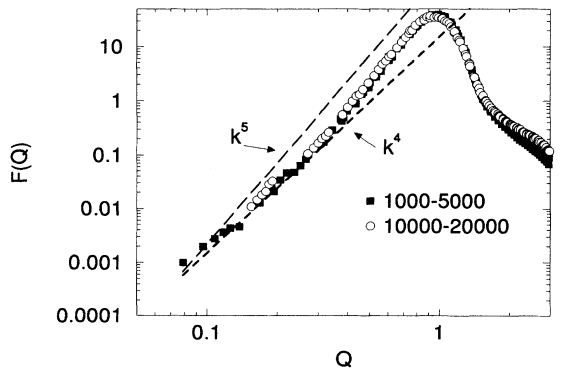

FIG. 26. Log-log plot of $F(Q)$ vs Q for regular binary-alloy simulation data. The small-k region is consistent with the k^4 hypothesis. For $0.4<Q<0.8$, the form factor is even steeper than k^4.

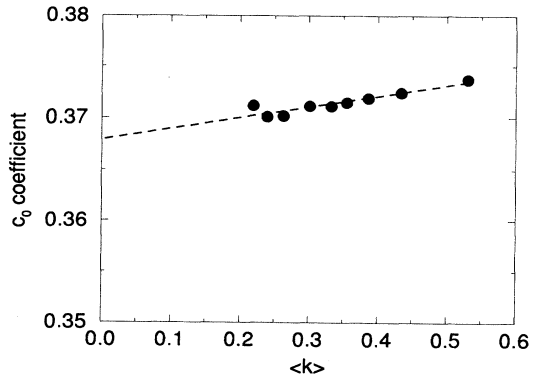

FIG. 28. Plot of the constant term c_0 vs $\langle k\rangle$ of $E(\rho)$ described in the text, determined by a least-squares fit to data in Fig. 27. Black dots are fitted values. Linear regression, represented by the dashed line, is used to estimate the asymptotic value of c_0 to be 0.368.

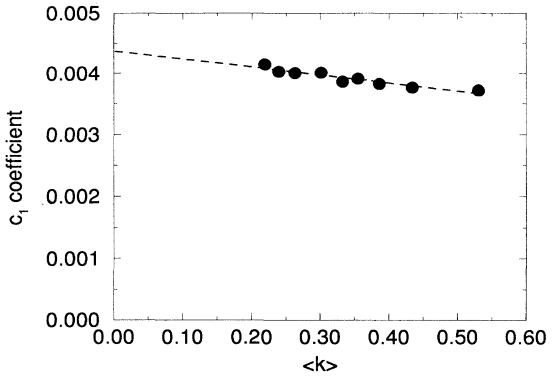

FIG. 29. Plot of the constant coefficient c_1 vs $\langle k \rangle$ of $E(\rho)$ described in the text, determined by least-squares fit to data. Black dots are fitted values. Linear regression, represented by the dashed line, estimates $c_1 = 0.004\,37$.

of $F(Q)$, we use the hardened data of $F(Q)$ for $0.8 < Q < 5$.

(iii) For small Q, we arbitrarily use the regular $F(Q)$ for $Q < 1.5$. That done, we extrapolate further by matching $20Q^4$ to the numerical data to generate the small-Q region.

We merge the sets of data together. Features (ii) and (iii) are merged by matching the overlapping peaks of $F(Q)$ from each part. All the numerical data is smoothed by a cubic-spline smoothing routine, and a final numerical form factor is generated with small- and large-Q behaviors obeying the known asymptotic laws. The results are shown in Figs. 45–47 with the corresponding binary-fluid results. An interesting result of this exercise is $G(\rho)$. We now can compare the collage $G(\rho)$, which should not suffer from any finite-size effects, with the numerical data. Again, to critically compare $G(\rho)$, we look at $\rho^2 G(\rho)$. This is done in Fig. 31. The collage $G(\rho)$ in comparison with the numerical data indicates the limit of our resolution of $G(r)$. The agreement is very good through the range $r\langle k \rangle < 10$, and, sensibly, the large-ρ behavior of the collage $G(\rho)$ is intermediate to the wildly varying numerical data.

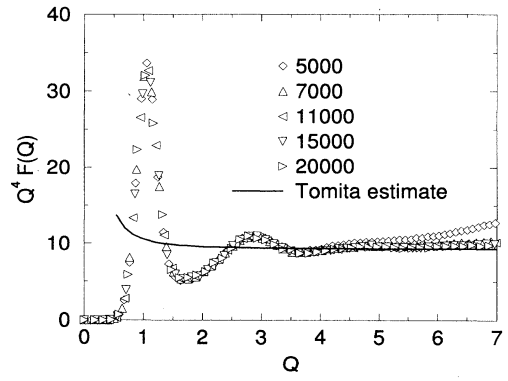

FIG. 30. Plot of hardened $Q^4F(Q)$ data vs small-Q generalization of Porod's law due to Tomita. Note that the latest times appear to merge with the asymptotic estimate at about $Q = 5$.

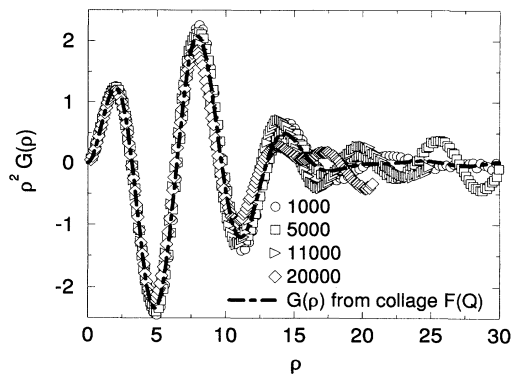

FIG. 31. Plot of $\rho^2 G(\rho)$ of collage data, compared to data obtained directly. The decay of the large-r region of $G(r)$ is comparable to that of the hardened $G(r)$ data of time step 1000.

B. Binary fluid at critical quench

In our study of binary-fluid spinodal decomposition, we use the CDS hydrodynamic model, [(21) and (22)] with velocity update skipping. We have four 192^3 samples in the study. The map is the same approximation to the tanh map as was used in the binary-alloy study. The parameters are $A = 1.3$, $D = 0.7$, $M\Delta t = 1.0$, and $\eta/\Delta t = 1.0$. The fixed points for the map are $\psi_{\text{bulk}} = \pm 1.047$. Each sample is started from random initial conditions uniformly distributed in $[-0.05, +0.05]$. Each sample is run to $t_{\text{CDS}} = 7500$ and sampled every 250 time steps to calculate $G(r)$ and $S(k)$. Figure 32 shows a three-dimensional picture of the isosurface $\psi = 0$ over several time steps. Comparing with Fig. 16, we see that the fluctuations in the thickness of the patterns are larger than in binary alloys.

The evolution of the probability density distribution of ψ is plotted over time in Fig. 33. At the earliest time plotted, $t_{\text{CDS}} = 500$, the system is not yet well separated. Figure 34 shows the evolution of $G(\rho)$ over time. The result of the hardened $G(\rho)$ is plotted in Fig. 35. At this level, the scaling holds remarkably well, but, in detail, some subtle deviations can be found. Finite-size effects can clearly be seen for $t_{\text{CDS}} = 3000$ from the plot of $\rho^2 G(\rho)$ in Fig. 36.

Close inspection of $\rho^2 G(\rho)$ in Fig. 37 shows that there are two different groupings of data. The early-time data from $t_{\text{CDS}} = 500$ and 1000 are clustered away from the rest of the data. The later time data from $t_{\text{CDS}} = 1500$–3000 do not quite stabilize into a scaling form, although they cluster distinctly from the earlier time data. This is probably an evidence of a slow crossover behavior discussed in Sec. VI B.

In Fig. 38, we plot $F(Q) \equiv \langle k \rangle^3 S(k)$ versus $Q \equiv k/\langle k \rangle$ over a range of time. Due to the effectiveness of flow in coarsening the domains, we are able to see a wide range of $\langle k \rangle^{-1}$. Note in this figure that there are only three points about the peak at the latest times shown. The conventional $\langle k \rangle$ can be distorted by the resolution of the peak of $S(k)$. As presented above, this is why we wish to use a $\langle k \rangle$ which is not badly affected by the discrete nature of the spherically averaged $S(\mathbf{k})$.

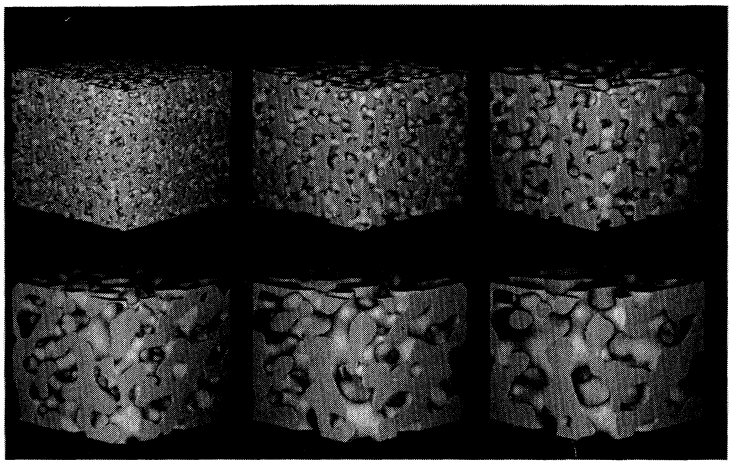

FIG. 32. $\psi=0$ isosurfaces of three-dimensional incompressible binary-fluid spinodal decomposition at critical quench. $\eta=1$, $M_{\rm CDS}=1$, and $D_{\rm CDS}=0.7$, using the tanh map described in the text with $A=1.3$. System size is 192^3. The entire 192^3 sample is exhibited. From top left to right, images are of $t_{\rm CDS}=500$, 1000, and 1500 data, and, from bottom left to right, of $t_{\rm CDS}=2000$, 2500, and 3000 data.

Examining the probability distribution for the order parameter (Fig. 33) shows that at $t_{\rm CDS}=500$ the order parameter is not well separated into different phases. The hardened form factor appears to scale well from times as early as time step 500. However, closer examination of the hardened form factor using the Porod plot in Fig. 39 shows that $t_{\rm CDS}=500$ does not quite scale with later times for $Q>2$. This is not unexpected from the behavior of $G(\rho)$. The other time steps appear to scale reasonably well for this quantity. The second hump in the Porod plot is now located at $k=2.7\langle k\rangle$.

Examination of a log-log plot of the hydrodynamic form factor in Fig. 40 shows that the small-k behavior is nearly fit by $k^{4.5}$ for $Q<0.5$. However, the exponent appears to be decaying toward k^4 at smaller Q. The small-k behavior has not been determined theoretically for the hydrodynamic model. If we assume that $S(k)$ is analytic about $k=0$, then the exponent must be 4 as long as the large-scale isotropy is preserved by the dynamics, as shown by Tomita [35]. Damage spreading in the binary-fluid system is contained by an exponentially decaying form similar to the binary-alloy case. Hence it is unlikely that the binary-fluid model induces inhomogeneities significantly greater than the binary-alloy dynamics, and is thus likely to obey the k^4 hypothesis.

As in the binary-alloy case, we extract more information from the small-scale behavior of $G(\rho)$. Figure 41 plots $E(\rho)\equiv[1-G(\rho)]\rho^{-1}$. To see in detail the evolution of $E(\rho)$, Fig. 41 shows a close-up view of $E(\rho)$. This data is fit to $E(\rho)=c_0-c_1\rho^2+c_2\rho^4$ using least squares. The coefficients c_0 and c_1 are plotted versus $\langle k\rangle$ in Figs. 42 and 43 and the asymptotic values are estimated by linear regression. The data for c_0 and c_1 show steady evolution as in the binary-alloy case, until about $t_{\rm CDS}=2250$, which corresponds to about $\langle k\rangle=0.14$. After this, the values of c_0 and c_1 fall. This is likely to be due to the finite-size effects that are affecting the large-ρ region of $G(\rho)$. In our analysis no special care has been taken for the data after $t_{\rm CDS}=2250$ (the effect is at most 5%, if any).

Ignoring time steps later than 3000, we estimate that the asymptotic value of $c_0=0.38$ and $c_1=0.0070$. The possible finite-size effect which affects the last few data points should not alter the values by more than $\pm3\%$ for c_0 and $\pm10\%$ for c_1. This translates into $A=0.38\langle k\rangle$ and $\bar{R}_m^2=4.5\langle k\rangle^{-2}$. Note that $\bar{R}_m^2$ is significantly

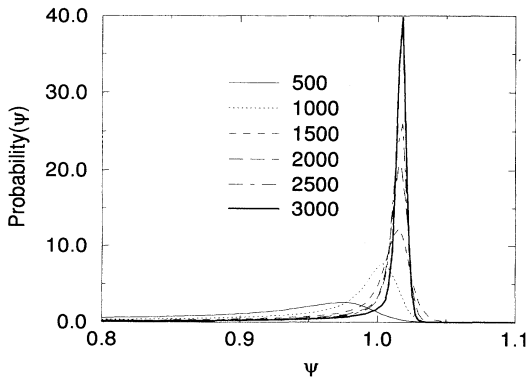

FIG. 33. Probability density distribution of ψ for the 192^3 binary-fluid system described in the text. Note that $\psi_{\rm bulk}=\pm1.04$. The bulk phases are well formed around $t_{\rm CDS}=1500$.

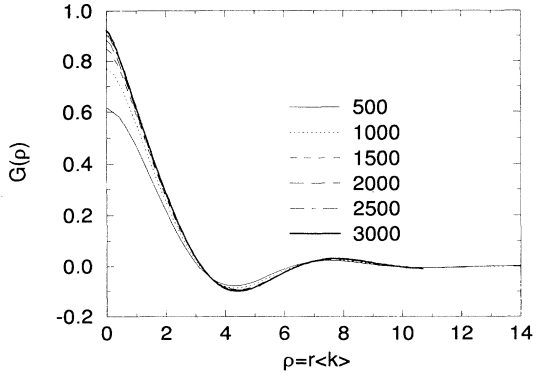

FIG. 34. Plot of $G(\rho)$ at various times for the 192^3 binary-fluid system. Due to the rapidity of the coarsening, the data for $t_{\rm CDS}=3000$ only go to $\rho\sim11$, which corresponds to $r\sim90$, the limit of half the linear system size.

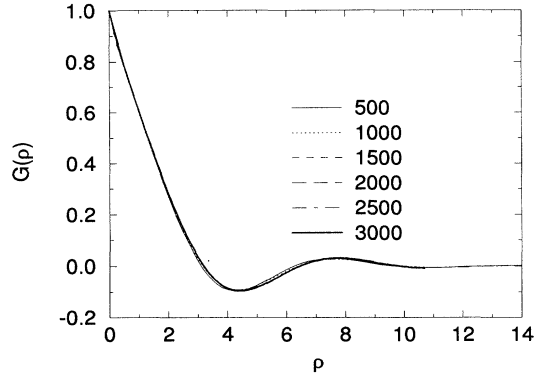

FIG. 35. Plot of $G(\rho)$ of hardened binary-fluid data. Scaling looks reasonably good for this function.

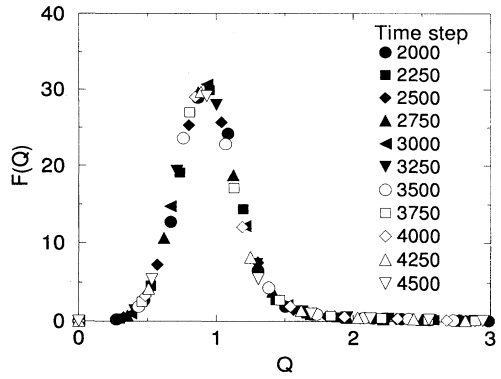

FIG. 38. Plot of form factor $F(Q)\equiv\langle k\rangle^3 S(k)$ vs $Q\equiv k/\langle k\rangle$ for times ranging from $t_{\mathrm{CDS}}=2000$ to 4500. Scaling appears to be well obeyed over the entire time range.

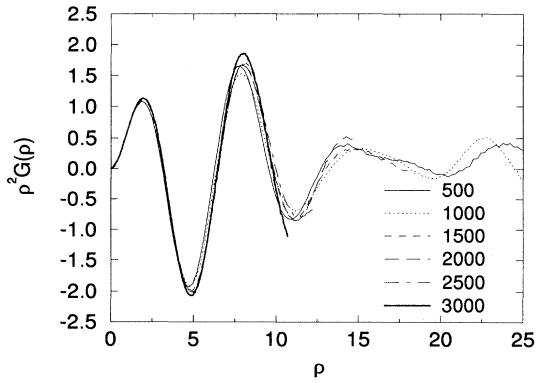

FIG. 36. Plot of $\rho^2 G(\rho)$ of hardened binary-fluid data. Unlike for the binary-alloy model, there appears to be some evolution of the first minimum over time. There may be some type of crossover in the dynamics.

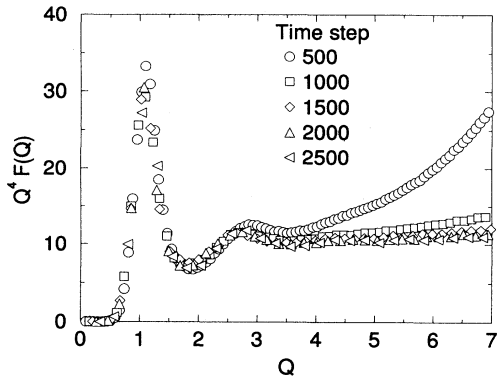

FIG. 39. Porod's plot of the hardened binary-fluid form factor.

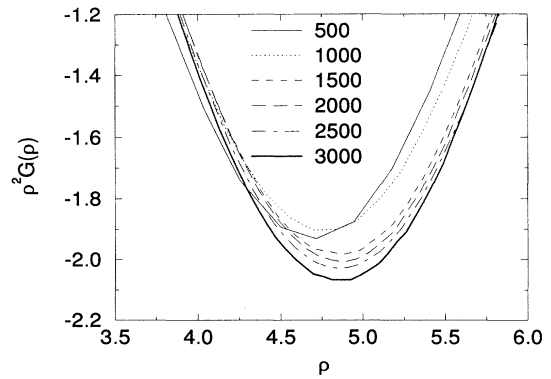

FIG. 37. Close-up plot of the first minimum of $\rho^2 G(\rho)$ of hardened binary-fluid data. Note that for $t_{\mathrm{CDS}}=500$ and 1000, the data cluster away from the later time data. The data for $t_{\mathrm{CDS}}=1500$ and later appear to belong to another cluster which slowly evolves.

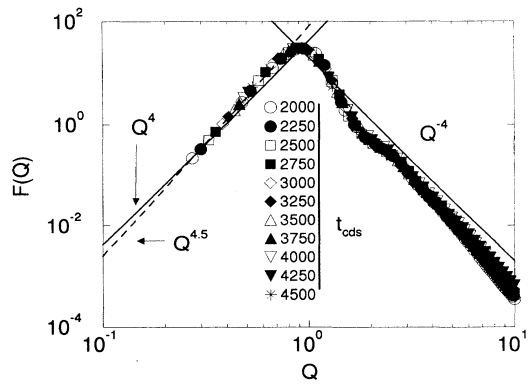

FIG. 40. Log-log plot of the binary-fluid form factor (regular) at various time steps. Note that at the latest times available, the form factor approaches a Porod's tail form for large Q.

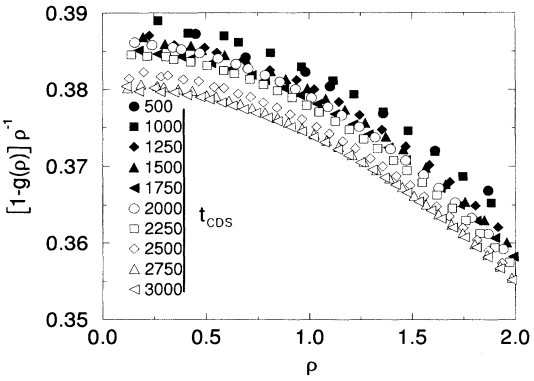

FIG. 41. Plot of $E(\rho)$ close up to the origin.

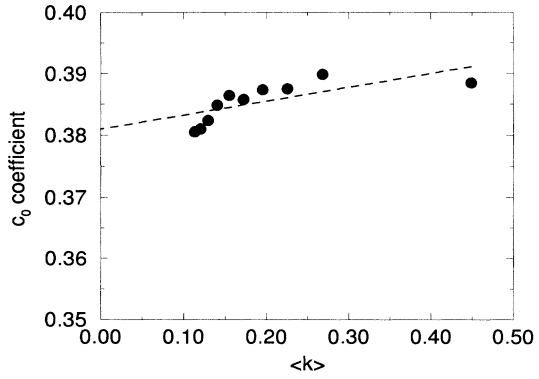

FIG. 42. Plot of the constant term c_0 of $E(\rho)$. The general trend is downward. The black dots are the coefficient from the least-squares fit, and the dotted line is the linear regression which estimates that, asymptotically, $c_0=0.381$. The last few points may be very much affected by the finite size of the system.

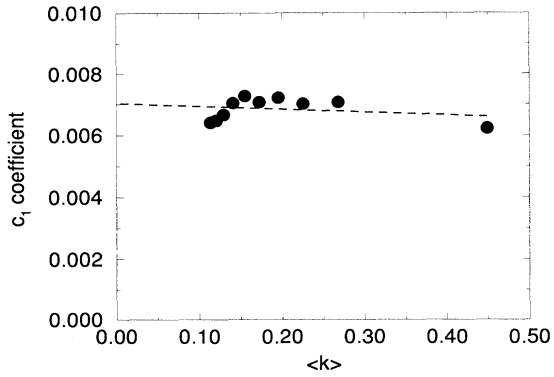

FIG. 43. Plot of the coefficient c_1 for the ρ^2 term in $E(\rho)$. Black dots represent the data least-squares fit, and the dashed line is the linear regression which estimates asymptotically that $c_1=0.0070$. Note that the general trend is upward as $\langle k \rangle \to 0$, but that the last few points behave like data taken for c_0 in Fig. 42.

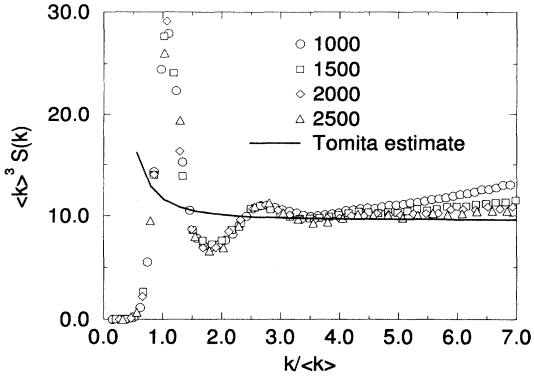

FIG. 44. Porod's plot of hardened data, and the Tomita estimate for the large-wave-vector tail of $S(k)$ using A and $\bar{R}_m^2$.

smaller than the value for the binary-alloy model for the same area density of interfaces. This is consistent with the more uneven looking configuration of the domains (Fig. 32). Large curvature regions occur together with small curvature regions, in contrast to a fairly even distribution of curvatures seen in the binary-alloy case. This is probably due to the stretching and compressing of tube-like domains under fluid dynamics. Figure 44 shows the hardened $Q^4F(Q)$ data plotted with the Tomita estimate for large Q using A and $\bar{R}_m$.

We form a collage $F(Q)$ and $G(\rho)$ the same way as in the binary-alloy case. From Fig. 40 we estimate $F(Q)=41Q^4$. We put together the hardened data for $0.8<Q<5.0$, discarding points that did not scale due to the jaggedness after hardening. Finally we used the Tomita estimate for $Q>5$. Data were merged together using a cubic-spline smoothing routine. The binary-fluid collage form factor is plotted in comparison to the binary-alloy form factor in Fig. 45. We note that the ratio of the peak half-width to the peak position is 0.45 for the binary alloy model and 0.54 for the binary fluid. Figure 46 shows a Porod plot, and Fig. 47 shows a log-log plot comparing the binary-alloy and binary-fluid collage form factors. Larger pattern thickness fluctuation in fluid sys-

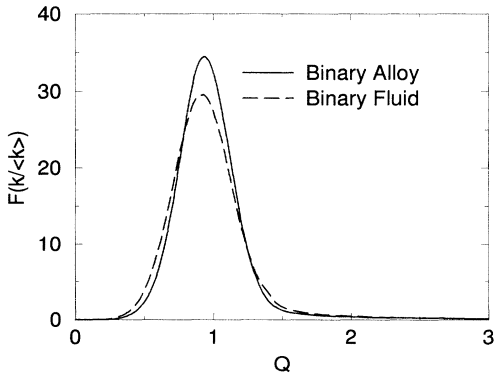

FIG. 45. Comparison plot of collage $F(Q)$ for binary alloys and binary fluids. Note that the fluid system has a broader form factor.

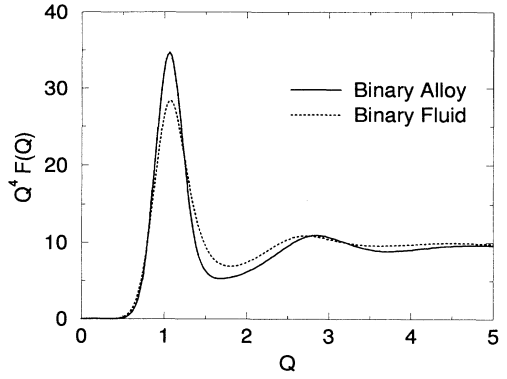

FIG. 46. Comparison plot of collage $Q^4F(Q)$ from binary-alloy and binary-fluid simulations. Fluid dynamics spreads out the fluctuations about the main peak in comparison to the binary-alloy dynamics, and the secondary peak is more diffuse.

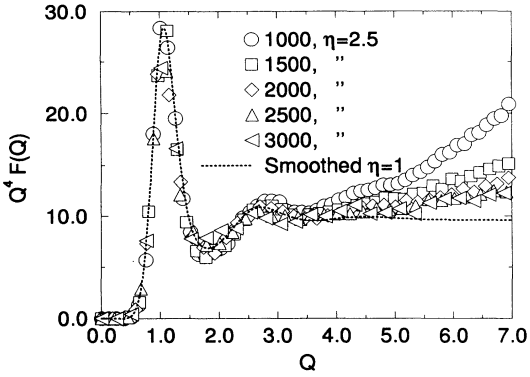

FIG. 48. Porod's plot comparison of collage $F(Q)$ for binary fluid with $\eta=1$ vs hardened $F(Q)$ data from various time steps of a 128^3 system with $\eta=2.5$, all other parameters being kept the same as in the $\eta=1$ simulations. Although finite-size effects may be significant in the 128^3 simulation, the difference is consistent with the subtle dynamical differences described in Sec. VI B.

tems is clearly reflected in the form factor.

The scaling of the form factor could be dependent on the viscosity of the fluid. In the case of binary-fluid phase separation in a Hele-Shaw cell [31], we found that the scaling form factor depended systematically on the factor $M\eta$, where M is the mobility, even when all other parameters of the system were fixed. In this case, the fluid dynamics and diffusive dynamics coarsened the system with the same asymptotic growth exponent as determined by dimensional analysis, so the balance between the two mechanisms determined the form factor. In the free 3-space fluid case, the fluid dynamic mechanism is clearly the dominant one for coarsening the system. Therefore, it might be reasoned that, at late times when fluid dynamics dominates, there is universal behavior independent of the factor $M\eta$. Hence we would believe that the form factor is not affected by changing the viscosity with all other parameters fixed.

We make a cursory inspection of this issue by comparing the collage form factor $F(Q)$ versus the hardened $F(Q)$ measured from a single 128^3 run with $\eta=2.5$ and all other parameters identical to our main 192^3 run with $\eta=1$. In direct comparison with $F(Q)$, we do not see much difference. Figure 48 compares the Porod plot of the $\eta=1$ collage form factor and the $\eta=2.5$ form factor. The data from the $\eta=2.5$ run generally follows the $\eta=1$ collage form factor. There is a small but systematic shift upward of the valley region at about $Q=2$ in exchange for a slight decrease in the main peak at later times for the $\eta=2.5$ data versus the collage $F(Q)$. Without more data at longer times and large system sizes, we may not be definitive on this. However, as we will see in Sec. VI B there is a good reason to believe that the $\eta=2.5$ system is dynamically better (or sooner) able to approach a true asymptotic regime than the $\eta=1$ system. In any case, it appears that the asymptotic form factor is invariant with respect to changing η.

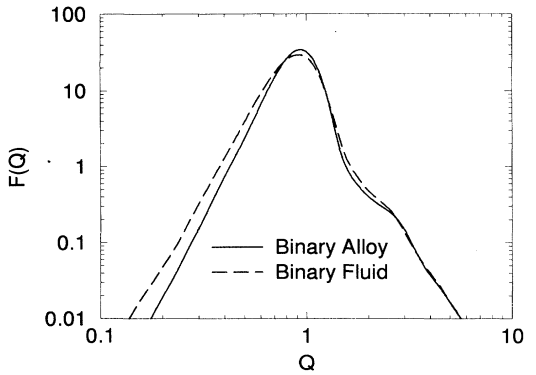

FIG. 47. Log-log plot comparing collage $F(Q)$ for binary-alloy and binary-fluid simulations.

C. Velocity-velocity correlation

Although the velocity field $\mathbf{v}$ is modeled as a slaved field [see (23)], it is still interesting to check the form of the velocity-velocity correlation function and check its scaling. We will look at $S_{vv}(k)\equiv\langle \mathbf{v}_{-k}\cdot\mathbf{v}_k\rangle$. Assuming that v scales like l/t, and that $l\sim t$ [65], we estimate that the average v^2 is a constant. This implies that $\int d^3k\langle \mathbf{v}_{-k}\cdot\mathbf{v}_k\rangle\sim C$. Using $Q=k/\langle k\rangle$, we get a dimensionless function $F_{vv}(Q)=\langle k\rangle^3 S_{vv}(k)$. If scaling holds, we expect $F_{vv}(Q)$ to be time independent.

The small-Q region of $F_{vv}(Q)$ fluctuates wildly from time to time and sample to sample, and the function decays very rapidly. Scaling is not easy to see. The log-log plot of $F_{vv}(Q)$ is given in Fig. 49, where the smallest k data point is removed since it is drastically affected by the finite size of the system and the periodic boundary conditions. We plot data from $t_{\rm CDS}=1500$ and on, since this is the point where the bulk is well formed, as seen in the probability distribution of ψ (Fig. 33). In this plot, we can see the scaling behavior as predicted. The most interesting aspect is the apparent power-law behavior of the large- and small-Q regions with a sharp transition in be-

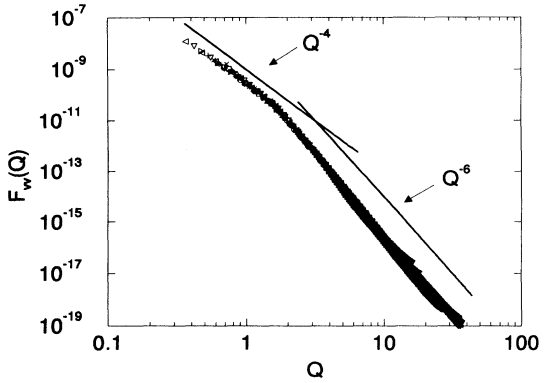

FIG. 49. Log-log plot of $F_{vv}(Q)$ from $t_{\mathrm{CDS}}=1500$ on. The smallest k data point was omitted from each time-step datum. Note that the curves all scale together very well and have a small-Q behavior of Q^{-4} and a large-Q behavior of Q^{-6}.

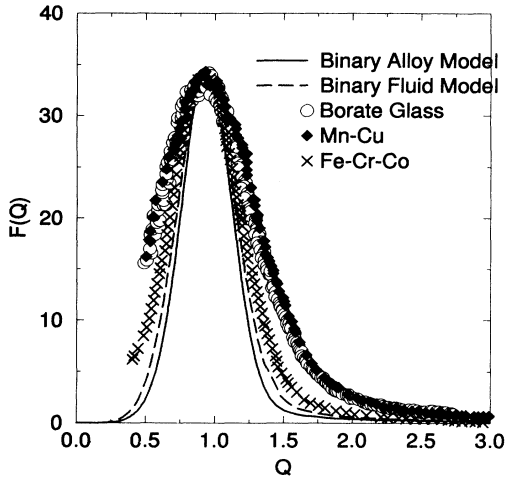

FIG. 50. Form factors from digitized published data of various binary-solid experimental studies. All form factors were normalized to the binary alloy model peak. The binary-alloy and binary-fluid model data are the collage $F(Q)$ for critical quench. The borate glass [16] and Mn-Cu system [13] are critical quench. The Fe-Cr-Co system [12] is off critical, but appears to have nearly the morphological structure of our critical quench studies.

tween. The small-Q region behaves like Q^{-4} until about $Q=1.7$, where it turns sharply over to Q^{-6} behavior. The large-k power-law behavior is consistent with a generalized Porod's law for a $n=3$, $d=3$ vector order parameter as described by Bray and Puri [36] and Toyoki [37]. In this case, it is predicted that the large-k region will behave like $k^{-(d+n)}$ in general, at least for $d \geq n$ (see also [66]). The small-k behavior seems clear, but we have no explanation for the power law. It should be pointed out, however, that $F_{vv}(Q)$ does begin to turn down at very small Q, although hardly noticeable.

The fact that the form of the velocity field correlation settles to an asymptotic form is consistent with a type of scaling regime associated with the morphology of domains independent of the finite wall thickness. The velocity fields are probably not much affected by wall thickness as long as the wall and the bulk are well formed. We note that from the probability distribution shown earlier than this is the case after $t_{\mathrm{CDS}}=1000$, explaining why velocity data from time steps 1000 and earlier did not scale well. The velocity field has very large small-wave-vector components. Their effect is easily seen in 3-space visualizations of the time development of a sample. The entire system appears to be unfolding as it coarsens, and large regions of the binary fluid move together. Consequently, domains are sometimes forced to merge or stretched apart by the fluid flow. Such global flows are strongly sample dependent, but do not affect the phenomena at the pattern size scale, so long as L/L_I is large.

D. Comparisons with experiments

1. Binary alloy

Ideal binary-solid systems appear to be difficult to realize experimentally. It is necessary to find a system which is isotropic without any volume change due to compositional change or any concentration-dependent shear or bulk modulus which would induce strain effects. Figure 50 compares our collage form factors for the binary-alloy and binary-fluid models against the experimental form factors from a borate glass system [16], a Mn-Cu system [13], and an off-critical Fe-Cr-Co system [12]. All the experimental data were obtained by digitizing data points from published figures. The authors apologize for any errors in digitizing the published data. All the form factors were roughly peak normalized to the peak of the binary-alloy collage form factor.

The borate glass system appears to be an ideal system in principle. It has no crystalline anisotropy. The data shown in Fig. 50 are a near critical quench. However, the growth exponent attained for the critical quench is only $0.24 \sim 0.26$. Another odd fact, pointed out by Craievich, Sanchez, and Williams [16], about the glass system, is that the width of the form factor decreases and the asymptotic growth exponent goes from $\frac{1}{4}$ to $\frac{1}{3}$ as the off-criticality is increased. Other numerical studies [23] have observed that the form factor width increases with increasing off-criticality, as have we in small-scale test studies. The general trend over a large set of studies is for the form factor to broaden as the system is more off-critical [67]. Further, in the Fe-Cr study, they note that the form factor becomes significantly narrower after the growth law crosses over from $\frac{1}{6}$ to $\frac{1}{3}$ behavior. This leads us to believe that the borate glass system may have quite different dynamics than that of the CH type, or that the critical quenched glass system is not yet in the asymptotic regime.

The Mn-Cu system also appears to be suited for comparison, since it is believed to have little strain effect. The growth law appears to be $t^{1/3}$. The form factor for the critical quench appears to match that for borate

glass, although both systems have different asymptotic exponents. In this case crystalline anisotropy is probably relevant. Spherical averaging of a single anisotropic crystal would certainly broaden the form factor. Even an isotropic scattering function could be due to a macroscopically isotropic arrangement of anisotropic crystals. Surprisingly, both the Mn-Cu and borate glass critical quench form factors are very much the same, although, as pointed out above, the systems appear to be very different. They are both significantly wider than either the binary-alloy or binary-fluid collage form factor.

The Fe-Cr-Co system [12] whose data is plotted in Fig. 50 was off-critical with a minority percentage about 30%. However, this form factor is definitely narrower than the above critical quench experiments, and the asymptotic growth rate appears to be $t^{1/3}$. Ion-field micrographs of the Fe-Cr-Co system [68] show the characteristic intertwining of domains such as what we observe for the critical quench, and shows the atomic structure to be very isotropic. This system may be much more representative of the ideal binary-alloy spinodal decomposition. A long-time critical quench study of this tertiary system, if possible, would be of interest in order to clarify many issues.

We do not compare any theoretical results [69–71] with our result because, unfortunately, all violate some asymptotic theoretical results such as conservation, sum rules, etc., or cannot be taken seriously at the late stages.

2. *Binary fluid*

The situation in the binary-fluid case is much better. The form factor for both simple and polymeric fluids appears to match reasonably well with our numerical data. One expects that there are of course no lattice anisotropy or shear modulus effects. In the case of the polymeric fluids, extensive and accurate data in the high-wave-vector region is available.

Figure 51 shows a comparison for the form factor from an isobutyric acid and water system [17], and from a lutidine and water system [18], both undergoing critical quench. Both studies report growth laws compatible with $l(t)\sim t$. Both sets of data had fairly large fluctuations in the actual form factor measurements, so the digitized data is taken from the published smooth interpolating fit to the experimental data. Further, the data did not extend into the large-wave-vector region beyond $1.8\langle k\rangle$, so it is not possible to compare Porod's plots. However, the data are significantly closer to agreement with the fluid collage form factor than in the binary-alloy case.

In Fig. 52, we see very good agreement between our fluid data and polymeric fluid data at critical quench. In this case, we digitized data from a study of a deuterated and protonated polymer mixture (D-H) [20], and for a polybutadiene and polyisoprene (PB-PI) mixture [72]. The data from polymeric fluids is in general of better quality than the data from binary-fluid and binary-alloy systems. We note that the curvature of the form factor in the $1.25\langle k\rangle - 1.75\langle k\rangle$ region of both polymeric fluid systems matches that of our binary-fluid model, and is clearly different from the binary-alloy model.

The Porod plot is shown in Fig. 53. Here we normalized the Porod tail to have the same amplitude, and shifted the vertical axis by a constant to set the tail level to zero. The best-quality data available are clearly in the PB-PI system, and they are also the closest fit to our simulation data. At the level of the Porod plot, the agreement is close but not perfect. The difference between the binary-fluid collage form factor and the experimental results consists of a shift downward of the main peak in exchange for a lift in the valley located around $2\langle k\rangle$. Such a difference was also noted in the comparison of our $\eta=1$ and 2.5 run. As we will see later in the discussion of the growth law for the binary-fluid model, this is likely to be an evidence of a subtle preasymptotic behavior which could occur in fluid systems. To check this behavior of the form factor quantitatively for the $\eta=2.5$ system, we will need to pursue simulations of size larger than 256^3. The small-k power-law behavior of the

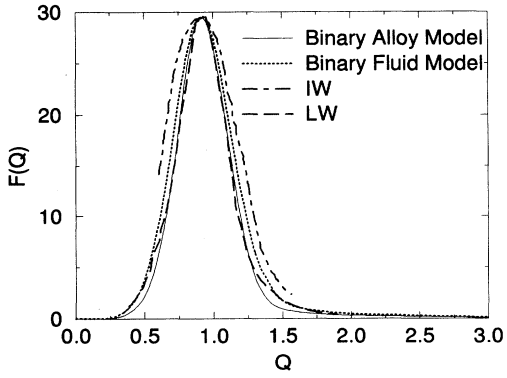

FIG. 51. Plot of form factor data of simple binary fluids digitized from published data in comparison to the binary-fluid model collage $F(Q)$. Experimental systems plotted are isobutyric acid and water (IW) [17] and lutidine and water (LW) [18]. Form factors are normalized to the peak of the binary-fluid model form factor.

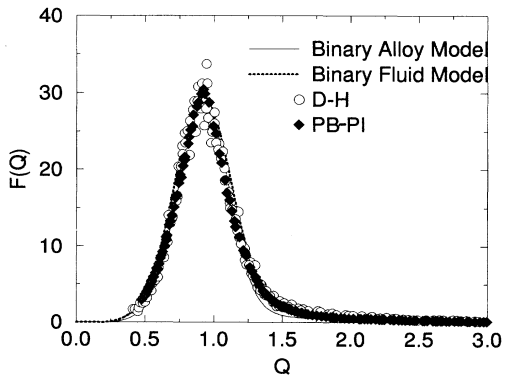

FIG. 52. Plot of form factor data of polymeric fluid digitized from published data in comparison to the binary-fluid model collage $F(Q)$. Experimental systems are a deuterated and protonated polymer mixture (D-H) [20] and a polybutadiene and polyisoprene mixture (PB-PI) [72] at critical quench. The form factors are normalized to the peak of the binary-fluid form factor.

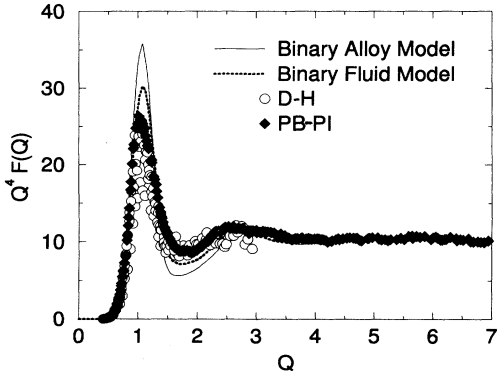

FIG. 53. Porod's plot of polymeric fluid and binary-fluid model data. Normalization of the peak position was retained from the previous figure and the height was normalized roughly so that tail regions coincided. Note the good qualitative agreement between the PB-PI system and the binary-fluid model. There is a slight systematic decrease in the peak in exchange for a slight upward shift in the valley at $Q\sim 2$. This is probably due to the nonasymptoticity of our result discussed in Sec. VI B.

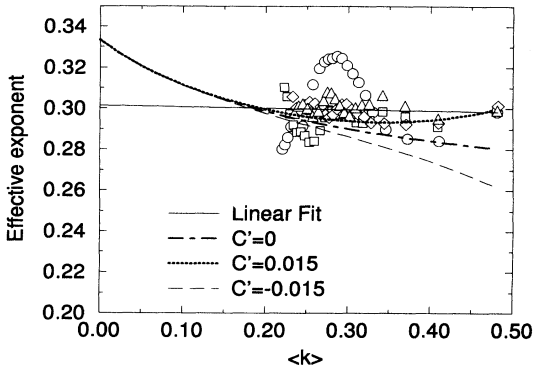

FIG. 54. Plot of the effective exponent of the 192^3-sized, tanh map system with $A=1.15$ and $D=0.7$. White symbols are measured effective exponents for the four different samples. Dispersion-relation-based growth laws with $C'=0$, 0.015, and -0.015 are superposed to illustrate the range and nature of variation of the growth law determined by the single parameter. These data are already in the strongly fluctuating regime due to the finite-size effect, as we see comparing with the subsequent figures, so no definite match is allowed, but the plotted growth law explains the leveling off of the exponent at sub-$\frac{1}{3}$ value.

form factor has a slightly greater exponent than 4. For the range of about $0.65\langle k\rangle - 0.9\langle k\rangle$, the D-H system was measured by Bates and Wiltzius to have a behavior of $S(k)\sim k^{4.5}$, which is in agreement with our findings as shown in Fig. 40.

Recently, Takenaka, Izumitani, and Hashimoto [52] demonstrated that all of the growth laws they found for a PB-PI system can be collapsed by appropriate time and length scale changes. The required changes are molecular weight dependent, but we may conclude, as discussed in Sec. III B, that polymer effects so far observed are all quantitative in the sense that they can be scaled out.

We are satisfied that we are on track to capture the experimental situation of critical quench binary-fluid decomposition, though we are not so satisfied in the binary-alloy situation. It is clear that the Porod-type plot is valuable in identifying subtle differences in experimental systems and numerical simulations. We hope that future experiments, particularly with solid systems, will detail enough data to successfully discern the form factor at the level presented here.

VI. GROWTH LAWS

A. Growth law of the binary-alloy system

While the asymptotic growth exponent of $\frac{1}{3}$ is generally accepted for spinodal decomposition in binary-alloy-like systems without strain effects, computational studies have fallen short of showing explicit asymptotic behavior. Upon close examination, we find, for example, that the effective exponent appears to be systematically less than $\frac{1}{3}$ during the range of the simulation. A simple linear fit to the plot (see Fig. 54) of the effective exponent $\alpha\equiv -\partial \ln\langle k\rangle/\partial \ln t$ versus $\langle k\rangle$ can sometimes project an asymptotic exponent close to $\frac{1}{3}$, but this is not at all satisfying. The fit depends crucially on the time range of the points chosen to be fit, and the linear extrapolation is not justified when the empirical exponents are significantly less than $\frac{1}{3}$. Due to the finite size of the system, α fluctuates more and more dramatically at late times, or for small $\langle k\rangle$. However, at earlier times, $\langle k\rangle$ does not appear to fall well on the linear extrapolation. Choosing only very late times for the fit leads to extremely unreliable results. Choosing all times tends to make the fit predict a too small asymptotic exponent. Thus we need a better understanding of the preasymptotic behavior of the growth law.

Since the order parameter is conserved, in order for the morphology to change, there must be order-parameter transport. This is essentially a diffusion process, so its characteristic time is $l(t)^2$, which is much smaller than that for the pattern coarsening. Hence, once the system is settled into some sort of self-consistent morphology, and scaling begins to occur, the entire morphology is governed by the strengths of sources and sinks of the order parameter which are the small fluctuations of the interface. The most natural consequence is that the decay rate of the relevant fluctuations at the interface determines the evolution of the system, so, on the average, $\omega(k_r)\sim t^{-1}$ determines the (pre)asymptotic growth law, where $\omega(k)$ is the dispersion relation of the (flat) interface, and k_r is the representative wave number of the interface fluctuation governing the evolution. We allow there to be a constant t_0 which accounts for an initial offset of the growth law due to the noncoarsening initial stages of decomposition. We already know that the scaling of the form factor is very good in the preasymptotic regime, so k_r must be proportional to $\langle k\rangle$: $k_r = B\langle k\rangle$.

This wave number must be larger than $\langle k \rangle$, because this must corresponds to the fluctuations on the curved interface whose curvature radius is, on the average, $l(t)$. We use the flat interface dispersion relation for the same reason. Thus we get a growth law

$$t - t_0 = C\omega(B\langle k \rangle)^{-1} , \tag{45}$$

with an appropriate constant C. When we look at a Porod plot of the hardened form factor (Fig. 34), which starts to scale well before the regular form factor does, we notice the large second hump roughly at $k_r = 2.9\langle k \rangle$. We hypothesize that this reflects a characteristic set of small fluctuations from the smooth interfacial wall. Thus we choose $k_r = 2.9\langle k \rangle$ to be a sort of constitutive equation.

Recently [39], we have found that the linear dispersion relation for the relaxation of fluctuations on the interface governed by the CH-type equation has a near-universal form dependent on the local free energy only through the interface thickness calculated by

$$\xi = \frac{\left[\int_{-\infty}^{\infty} dz\, \psi'(z)\right]^2}{2\int_{-\infty}^{\infty} dz\, \psi'^2(z)} , \tag{46}$$

where ψ is the kink solution. The dispersion relation for $k\xi < 1.0$ is very nearly of the form

$$\omega(k) = Mk^3 \frac{1}{\xi}(1 + ck\xi) , \tag{47}$$

where $c \approx 0.66 \approx 2/3$, k is the wave vector of a small fluctuation on a flat interface, and M is the mobility of the system. From (45) and (47) we can calculate the effective exponent as a function of $\langle k \rangle$ as

$$\alpha(\langle k \rangle) = \frac{3 + 2B\langle k \rangle\xi}{9 + 8B\langle k \rangle\xi}\left[1 + C'(B\langle k \rangle)^3 \frac{3 + 2B\langle k \rangle\xi}{3\xi}\right] , \tag{48}$$

where $C' = CMt_0$. Here we computed ξ with a discrete version of (46), numerically solving for an equilibrium wall configuration.

We compute the effective exponent for actual simulations by

$$\alpha(\langle k \rangle(t_i)) \approx -\frac{t_i}{\langle k \rangle(t_i)} \frac{\langle k \rangle(t_i) - \langle k \rangle(t_{i-1})}{t_i - t_{i-1}} . \tag{49}$$

We try a one-parameter fit to (48) of the empirically obtained exponents using C' described above. In practice, we do the fit by eye. At this point, we do not attempt a strict quantitative analysis since the measured effective exponents are very noisy, but we wish to investigate the validity of the above formulation and its relationship to scaling.

We do the fit for our main 192^3 simulation using the tanh map described before. The simulation parameters are $A = 1.15$, $D = 0.5$, and $M = 1.0$. This gives $\xi = 1.39$ in lattice units. In Fig. 54, we see that the effective exponents calculated from each of the four samples fluctuates considerably, but that they are consistently below $\frac{1}{3}$. The linear fit estimates $\alpha = 0.301$. While the fluctuations do not allow a definitive match, the plotted growth law with $C' = 0$, 0.015, and -0.015 are consistent with the raw data. This explains the leveling off of the exponent at a sub-$\frac{1}{3}$ value, preceding a steady rise toward $\frac{1}{3}$ which is beyond the capability of our computation to attain. The fit does not look very good in this case because for these data $\langle k \rangle$ is already too small, as we will see generally below.

Figures 55–57 demonstrate that the above finding is not fortuitous. Figure 55 plots the effective exponent for the tanh map system of $A = 1.3$ and $D = 0.7$. This is an extreme case where the measured exponent has an early maximum of 0.38, then a dramatic fall to a minimum of 0.30. Using the single adjustable parameter, we can successfully match the effective exponents even in this case. It should be noted that the single parameter does not allow very much freedom in generating the effective exponent curve. Figure 56 plots the effective exponent for a single $D = 0.7$, 128^3 sample for the model with the following piecewise polynomial map:

$$\mathcal{F}(\psi) = \begin{cases} 1.25\psi - 0.15\psi^5 & \text{if } |\psi| < 0.7319 , \\ 0.2\psi + \mathrm{sgn}(\psi)0.8 & \text{if } |\psi| \geq 0.7319 . \end{cases} \tag{50}$$

This gives $\xi = 1.71$ for $D = 0.7$ and 2.16 for $D = 0.8$. Empirically we guess that the effective exponent for single 128^3-sized systems are well behaved until roughly $\langle k \rangle \sim 0.3$ or 0.4. This is consistent to the fact that for a set of 64^3 samples we tried, the effective exponent for the samples was already quite spread out by $\langle k \rangle \sim 0.6$. Figure 57 plots the effective exponent for two 128^3 piecewise polynomial systems with $D = 0.8$. One sample was allowed to run beyond $\langle k \rangle = 0.3$ and shows severe fluctuations after that point. The two systems are fairly close together until $\langle k \rangle = 0.3$.

In the above instance, the theoretical curve models the effective exponent after a certain $\langle k \rangle$ or time. It is in-

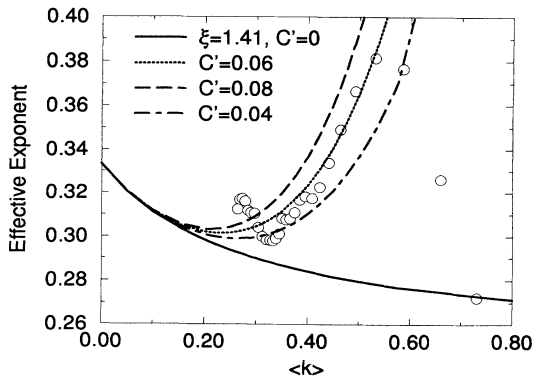

FIG. 55. Plot of the effective exponent of the 128^3-sized, tanh map system with $A = 1.3$ and $D = 0.7$. White circles are measured effective exponents for the sample. The dispersion-relation-based growth law is plotted with $C' = 0$ as reference. Growth is also plotted using $C' = 0.04$, 0.06, and 0.08. For the range $\langle k \rangle < 0.55$, these curves capture the behavior of the growth exponent. Note that data start to fluctuate significantly at around $\langle k \rangle = 0.35$. We attribute this to a finite-size effect.

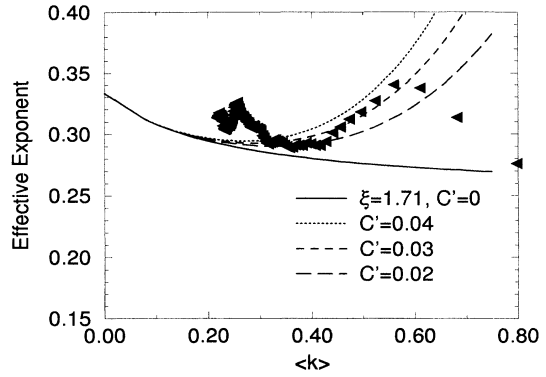

FIG. 56. Plot of the effective exponent of the 128^3-sized system using a piecewise polynomial map system with $D=0.7$. The black symbol is for the 128^3 sample. The dispersion-relation-based growth law is plotted with $C'=0$, 0.02, 0.03, and 0.04. Agreement with the growth law starts at approximately $\langle k \rangle=0.55$. At $\sim\langle k \rangle=0.3$, the growth law starts to fluctuate significantly.

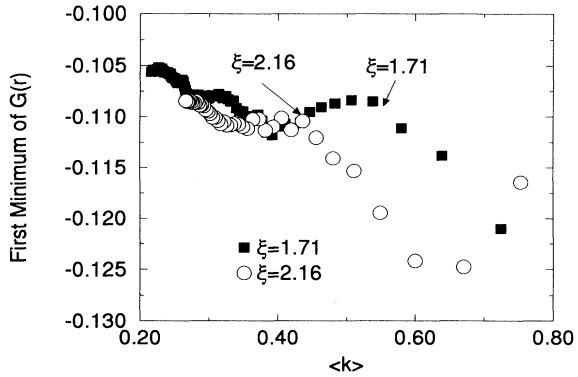

FIG. 58. Plot of the value of the first minimum of the hardened $G(r)$ for the single 128^3 sample run using the piecewise polynomial map with $D=0.7$ and the shorter of the two $D=0.8$ runs. -0.11 is roughly the value of the minimum when $G(r)$ is scaling. Note that -0.11 is achieved for both systems at the $\langle k \rangle$ at which they respectively start to agree with the growth laws based on the dispersion relation, as pointed out by the arrows in the figure.

teresting to see what importance is embodied by the start of agreement between the dispersion curves and the data. To do this, we generate more data to test the theory using the two piecewise polynomial maps. In addition to measuring $\langle k \rangle$, we gather the hardened $G(r)$ data to check scaling. To quantitatively check the scaling of $G(r)$ in a concise manner, we simply monitor the value of the first minimum of the hardened $G(r)$ and plot it versus $\langle k \rangle$. Ideally, the minimum should settle to a constant value if $G(r)$ is scaling.

In the $D=0.7$ case, the theoretical growth law starts to agree with the measured effective exponent at about $\langle k \rangle=0.6$. For the $D=0.8$ case, this agreement starts at about $\langle k \rangle=0.4$. In Fig. 58, the value of the first minimum of the hardened $G(r)$ is plotted for the two different D values. Note that for the $D=0.8$ or $\xi=2.16$ case the minimum approaches a plateau at about -0.11. This plateau starts at about $\langle k \rangle=0.4$. For the $D=0.7$, $\xi=1.71$ case, the minimum passes -0.11 at about $\langle k \rangle=0.6$ and fluctuates about that value. The fluctuations of the first minimum away from -0.11 roughly correspond to regions where the effective exponents fluctuate away from the most likely theoretical curve. Near $\langle k \rangle=0.3$, the measured effective exponent starts to be very much affected by fluctuations, and correspondingly, $G(r)$ deviates away from its scaling form as noted by Fig. 58. We suspect that some of these large excursions may be due to the abrupt change in the Euler characteristic of the system as it coarsens. For small systems the genus of the pattern is relatively small, and the loss of a connecting tube probably has greater effect in such a situation than in a large system with a large genus. Nonetheless, it appears that the start of good scaling corresponds with the start of agreement with the dispersion relation.

Thus a consistent picture has emerged. The growth law, beyond the point scaling starts, is governed by the decay rate of the small fluctuations of the interfacial wall.

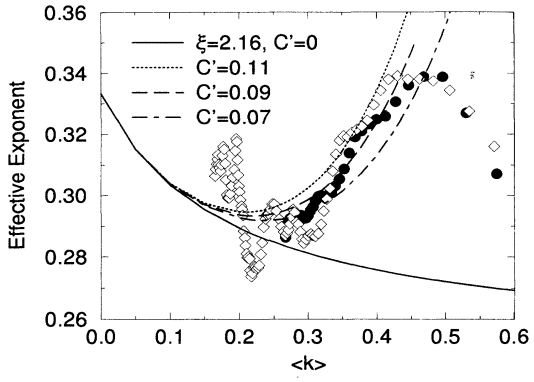

FIG. 57. Plot of the effective exponent of two 128^3-sized samples run using the piecewise polynomial map system with $D=0.8$. The white symbol represents the effective exponent of one sample allowed to run out beyond $\langle k \rangle=0.25$. The other sample ran only to $\langle k \rangle=0.25$, but was used to collect $G(r)$ data. The dispersion relation is plotted with $C'=0$, 0.07, 0.09, and 0.11.

B. Growth law of the binary-fluid system

From dimensional analysis, one expects to see $l\sim t$ [8,9]. Plotting the growth law $\langle k \rangle^{-1}$ versus time step (Fig. 59), we can clearly see the apparent effect of finite size on this measurement. The point in $\langle k \rangle$ at which finite-size effects take over scales roughly with the system size. From this point of view, it appears that the 192^3 system is reasonably free of finite-size effects up to $t_{\mathrm{CDS}}\sim 4000$. The growth law appears to be linear from about $t_{\mathrm{CDS}}=1000-4000$.

When we calculate the effective exponent (48) of our growth law as a function of $\langle k \rangle$, linear regression would predict an asymptotic exponent of ~ 0.8 (Fig. 60). It should be noted that, for small to medium times, a simple

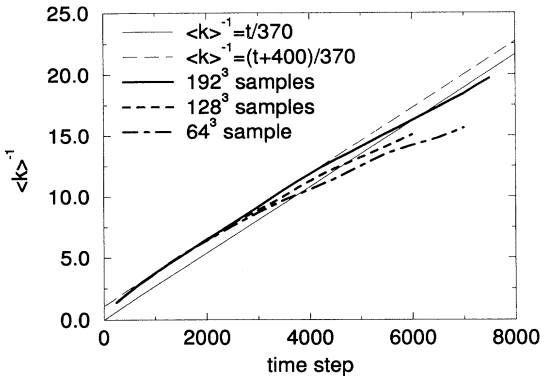

FIG. 59. Plot of $\langle k \rangle^{-1}$ vs time step for 192^3 and 128^3 data with four samples each, and a single 64^3 sample for the binary-fluid model. An approximate tanh map was used, with $A=1.3$, $D=0.7$, $M=1.0$, and $\eta=1.0$.

growth law such as $l(t) \propto t - t_0$ would show an effective exponent much less than 1. This is due to the sensitivity of a log-log plot to the presence of constants or other non-power-law contributions to $l(t)$. The hydrodynamic system coarsens rapidly, and easily reaches an almost fully phase separated state in a small volume studied computationally. Consequently, the sums used in the calculation of the length are dominated by a few points in **k** space, so that the calculated effective exponent for small $\langle k \rangle$ fluctuates wildly at later times. Figure 60 clearly shows all these difficulties.

To clearly illustrate the nature of the errors, we make a simple model curve with small fluctuations in order to simulate the above problems. First we posit that the growth law is generally of the form as $l(t)=at+b$, where a and b are constants. Next we compensate for the finite-size effect with a subtraction as $l(t)=at+b-ct^2$. Finally, we perturb our fitting form with a small perturbation $l(t)=(at+b-ct^2)[1+d\sin(\Omega t)]$, where d and Ω are constants. For the values of $a=0.0027$, $b=1.08$, $c=2.6\times10^{-8}$, $d=0.002$, and $\Omega=0.02$, this model $l(t)$ would not reveal very much variation from the $l(t)$ curve generated by $d=0$. Figure 61 generates an effective exponent plot of the test growth curve. This hypothetical effective exponent bears a striking resemblance to the scatter of the actual data and shows the difficulties of computing the effective exponent well. Therefore an asymptotic linear growth law is not in contradiction to our data, once finite size and some type of fluctuation are accounted for.

However, the above may not be the complete story. To make further progress, we try to understand the preasymptotic growth law in terms of the interface dispersion relation. This is natural, as in the binary-alloy case, because the form factor already scales well before the true asymptotic growth law is seen. Unfortunately, we do not have the same level of control over the dispersion relation as we did in the binary-alloy case [39]. A computational study of the dispersion relation for binary fluids is given in Ref. [40].

The results of the dispersion relation study [40] can be summarized as follows. Generally for any viscosity, the spectrum of the linearized operator consists of an essential spectrum and a point spectrum with a point corresponding to the Nambu-Goldstone (NG) mode. In Fig. 62 we plot k versus ω^{-1} for the NG mode and the bottom of the essential spectrum for the case $\eta=1$, $M=1$, $D=0.7$, and $A=1.3$ for the tanh map. Note for fixed k that the lower ω is to the right in Fig. 62. For large k the lower bound of the spectrum is the point spectrum corresponding to the NG mode, but for smaller k the lower bound is the lower limit of the essential spectrum.

The NG mode decays as $\omega \sim k$ for sufficiently small k, consistent with the growth law $l(t) \sim t$. However, the lower limit of the essential spectrum behaves like $\omega \sim k^2$, so that eventually the point spectrum goes into the essential spectrum for small k. The lower limit of the essential spectrum corresponds to that for the linearized CH operator [39]. A system with larger viscosity exhibits spectra closer to that for the binary-alloy system. There-

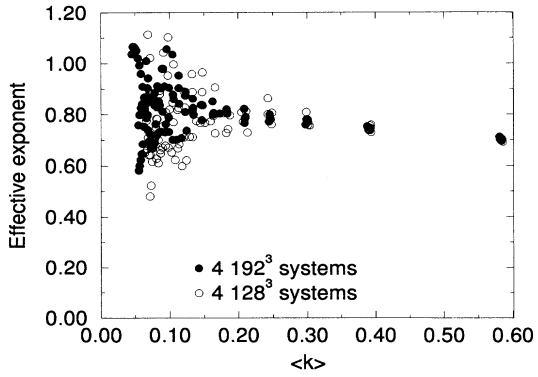

FIG. 60. Plot of the effective exponent vs $\langle k \rangle$ for 192^3 and 128^3 systems, each with four samples. The effective exponent of each sample is plotted. We note that if the effective exponent data of the 128^3 samples are rescaled on the $\langle k \rangle$ axis by $\frac{2}{3}$, then the width of the fluctuation envelope of the 128^3 and 192^3 data would roughly coincide.

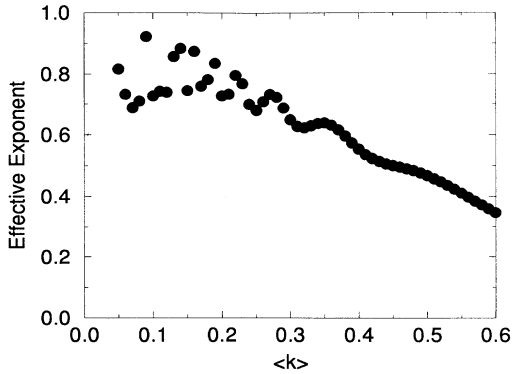

FIG. 61. Plot of the effective exponent of the simulated growth law described in the text. This points to the difficulty of obtaining the effective exponent if there is a small noise or a systematic measurement error.

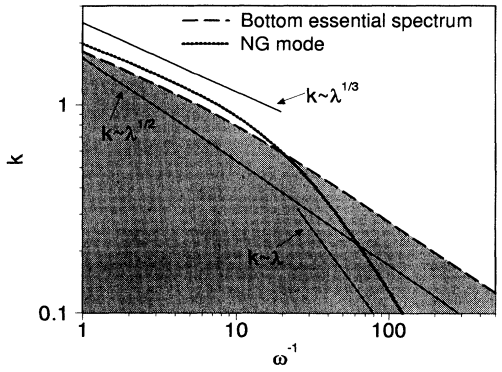

FIG. 62. Schematic description of the dispersion relation around the kink solution for the binary fluid with $\eta=1$. Plot of k vs ω^{-1} for $\eta=1$. The Nambu-Goldstone (NG) mode computed is represented by the dotted line. The dashed line is the bottom of the essential spectrum as estimated from the binary-alloy model. The gray area is the essential spectrum. Note the various power-law behaviors of the different branches in different regimes.

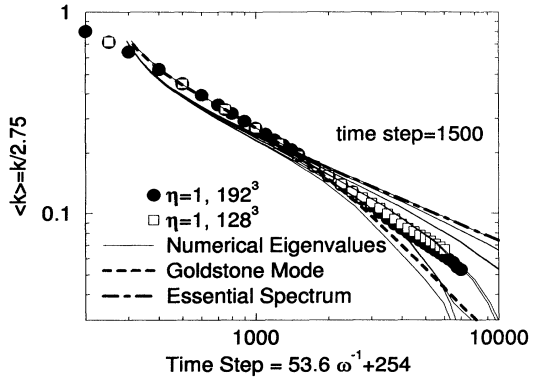

FIG. 63. Plot of the growth law for the $\eta=1$ case.

fore, if η is large, then the NG branch behaves essentially like $\omega\sim k$ when it hits the essential spectrum. If η is not very large, the NG branch will hit the essential spectrum before it reaches the asymptotic behavior of $\omega\sim k$. In the case of the $\eta=1$, the latter occurs. Thus the dispersion relation does not have universality with respect to the viscosity. This strongly suggests that the preasymptotic behaviors are sensitive to viscosity. This will be discussed at length below.

Since the spectrum does not have a clear separation into the point and essential spectrum in contrast to the binary-alloy case, we do not try to reproduce the growth exponent directly from the dispersion relation. Instead, we fit the measured growth law directly to the dispersion relation. The representative wave number of the interface fluctuation k_r must be proportional to $\langle k\rangle$, since even in the binary-fluid case the form factor becomes roughly scalable before the system reaches the true asymptotic regime. We note that the Porod plot for the fluid system (Fig. 46) has a second hump which is at a smaller $Q=k/\langle k\rangle$ than the binary-alloy system. The second hump in the fluid system appears to be at $Q=2.75$. Hence we set $k_r=2.75\langle k\rangle$. We relate ω and t analogously to the binary-alloy case as the $C\omega^{-1}=t-t_0$. t_0 was chosen by eye, with the criteria that as much of the dispersion curve match the experimental growth law as is possible (Fig. 63). We find that the growth law fits the NG mode very well until it hits the essential spectrum. After that point, the growth law appears to follow a path between that of the NG-like mode which obeys $\omega\sim k$ and the bottom of the essential spectrum which obeys $\omega\sim k^2$. We recall that the hardened $\rho^2G(\rho)$ does evolve slightly after time step 1500 (see Fig. 37). Time step 1500 corresponds to the point where the growth law evolves through the essential spectrum, as noted above.

As in the binary-alloy case, we wish to check if the above results are spurious. We check by fitting the growth law to the data of a single $\eta=2.5$ run of size 128^3, which ran with all other parameters identical to the main $\eta=1.0$ study. In Fig. 64 we exhibit a log-log plot of $\langle k\rangle(t)$ for $\eta=2.5$ in the dispersion relation form. On the same plot we fit the dispersion relation to the numerical growth law. After setting $k_r=2.75\langle k\rangle$, we obtain a good fit by eye by setting $t_{\rm CDS}=57\omega^{-1}+524$.

Now to check scaling, we note that the dispersion-relation-generated growth law starts to match the actual data at about $\langle k\rangle=0.4$ for $\eta=2.5$. We plot as before the first minimum of the hardened $G(r)$ as a function of $\langle k\rangle$. In Fig. 65, we see that it is at $\langle k\rangle=0.4$ that the first minimum reaches a plateau. At $\langle k\rangle=0.3$, the curve resumes rising, and this corresponds roughly to the point where the crossover knee in the NG mode dispersion relation starts. The region after $\langle k\rangle=0.2$ is dominated by a large fluctuation, and nothing firm can be said. However, it is conceivable that with better data, the first minimum of the hardened $G(r)$ reaches a new plateau corresponding to the region after the NG mode crossover. Our hypothesis is that the first plateau in Fig. 65 corresponds to the system evolving with the growth law controlled by the $k\sim\omega^{1/3}$ regime. Then there is a cross-

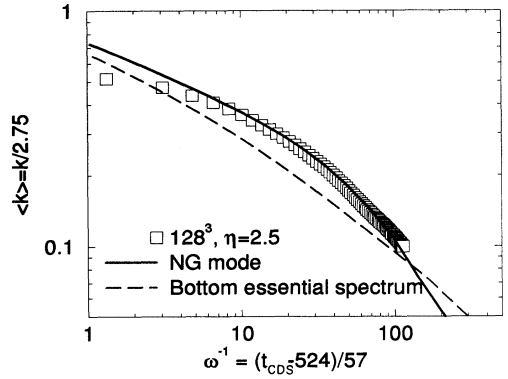

FIG. 64. Plot of the empirical growth law with the time step mapped to λ^{-1} as used in the dispersion relations. In this way one can clearly see the $\frac{1}{3}$ and 1 growth laws.

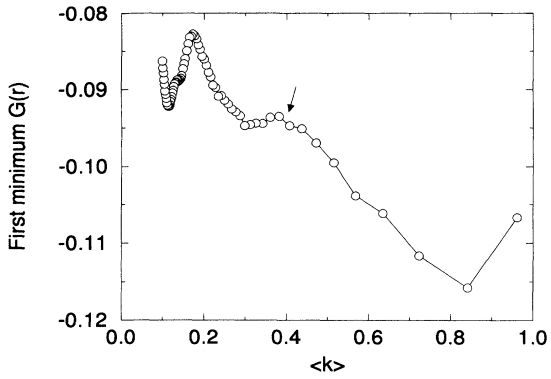

FIG. 65. Plot of the first minimum of hardened $G(r)$. The plot plateaus at about $\langle k \rangle = 0.4$, which coincides with the agreement of the dispersion relation growth law and the numerical data.

over to the $k \sim \omega$ regime corresponding to a rise in the first minimum of the hardened $G(r)$. Finally, there is the $k \sim \omega$ regime, where we conjecture Fig. 65 would have reached a new plateau. In the $\eta = 2.5$ case, we cannot extend the simulation into the essential spectrum region due to the system size limitations, but it is clear that the effective growth exponent continues to head toward -1.

For binary fluids the diffusion time scale $l(t)^2$ is much larger than the asymptotic growth time scale $l(t)$. This is diametrically different from binary alloys, and implies that diffusion may not be able to catch up with the displacement of the interface due to advection especially when viscosity is low. At earlier stages, this could delay the establishment of the true equilibrium bulk concentrations; a relatively mushy state would last considerably longer than the high viscosity cases. Actually, we have observed that with very low viscosity or mobility, $M\eta \sim 0.1$, the bulk did not reach its equilibrium value even though the domain pattern appeared well established. The bulk reached a magnitude of about 0.8, although the bulk equilibrium value should be 1. Eventually the bulk did appear to be rising toward 1, but during the time of the test simulation it did not reach 1. The effect appears to be independent of the size of the time step. Since fluid systems experience frequent reconnections of the domains with subsequent relatively rapid reorganization of the patterns, even at relatively later stages the bulk concentration may be lowered locally. This prevents the system from reaching its asymptotic regime quickly. This explains why the system with $\eta = 2.5$ seems to reach fluid dynamical asymptopia more easily than the $\eta = 1$ case despite the fact that fluid dynamical effects should be more dominant in the latter. Roux's [73] result, which exhibits a very clear crossover from the $\frac{1}{3}$ to the linear regime, may be understood from this point of view.

The above conclusion can be translated into the behavior of the dispersion relation: the exponent -1 is easily observable when the NG mode goes into the essential spectrum for as small k as possible. In [40], it is noted that the crossover region does not scale together when dispersion relations for the NG mode for several different η's are scaled together. This nonuniversality of the preasymptotic behavior of the growth law is due to the competition of the linear law with the "$\frac{1}{2}$" law corresponding to the essential spectrum $\omega \sim k^2$ but not with the $\frac{1}{3}$ law, especially when the viscosity is low. This is at variance with Furukawa's phenomenological growth law [41], which is a direct extension of Huse's attempt to understand the preasymptotic growth law for the binary alloys [74,33]. Close examination of published data often show that for certain experimental parameters, the actual agreement with Furukawa's law over the range of experiment is not that good. Only a collage of experimental data gives the appearance of a master curve. For polymer systems we can change viscosity widely by changing the molecular weight, so that the nonuniversality due to this interference becomes visible, but it is not a genuine polymer effect.

The numerical instability empirically occurs at the point in the simulation where the essential spectrum crosses the NG dispersion relation. This is true in the $\eta = 1$ case, as the adaptive $n_{v\text{skip}}$ function generally turns on at about $t_{\text{CDS}} = 1500$, which is the start of the essential spectrum region from Fig. 63. Relative to the fast fluid dynamic mode, the perturbed bulk does not quickly relax back to its equilibrium value. Bulk regions are sometimes away from their equilibrium value due to the disconnection and reconnection of domains, especially in the near-critical quench case. Unless a fine time step is used to track these regions, the fluid dynamic part of the simulation can quickly overreact to the distorted regions incorrectly, particularly since the establishment of a proper equilibrium bulk phase is so slow.

VII. CONCLUDING REMARKS

We have presented a systematic study of spinodal decomposition in critically quenched symmetric binary systems with and without fluid dynamical effects. We wish to summarize our main conclusions here.

(1) For binary alloys the asymptotic form factor can be obtained from a fairly preasymptotic results with the "hardening procedure" [30]. This implies that although the interface may not be sufficiently thin compared to the pattern size, and consequently the growth law may not be asymptotic, the spatial patterns are already statistically similar to the later stage patterns. For binary fluids, the hardening procedure gives an almost time-independent master form factor, but the small nonasymptoticity is still discernible with Porod's plot.

(2) We have given the best estimates of the asymptotic form factors in a collage form which is consistent with various asymptotic theoretical results (Figs. 45–47). We know from our previous studies and from the current study that these form factors are universal. For binary alloys, the form factor is independent of the choice of the free energy so long as the free energy is symmetric and gives one hyperbolic source and two hyperbolic sinks. No quantitative specification is needed, but only these qualitative features characterize binary alloy spinodal decomposition. For binary fluids, it is very likely that the

form factor is independent of the value of the kinematic viscosity as long as the $l(t) \sim t$ regime is reached. This is distinct from the Hele-Shaw binary-fluid spinodal decomposition [31]. The (viscosity-dependent) nonasymptoticity mentioned in (1) is almost harmless.

(3) The estimated asymptotic form factors exhibit clear difference between the binary-alloy and binary-fluid cases. The form factor for alloys is sharper and its Porod's plot has better defined secondary peak(s) than the fluid counterpart. This is consistent with the more uniform spatial patterns observed in alloys than in fluids.

(4) In contrast to the form factors, asymptotic growth laws are hard to obtain. Preasymptotic growth laws are found to be intimately related to the dispersion relation of the fluctuations around kinks. This is natural, since asymptotic patterns are formed in the preasymptotic stages, as demonstrated in (1), after which the entire pattern can coarsen due to the transport of materials whose sinks and sources are decaying small fluctuations of the interfaces.

(5) The essential spectrum of the interface dispersion relation has a crucial effect on the preasymptotic growth law of binary fluids. The competition between the Nambu-Goldstone mode and the essential modes dictates the crossover behavior which disagrees with Furukawa's proposal especially when viscosity is small. When viscosity is sufficiently large, however, the direct crossover from the $\frac{1}{3}$ to 1 regimes still may be observed.

(6) Damage-spreading studies clearly demonstrated that there is a unique length scale in spinodal decomposition, and that the size of the independent volume is given by the pattern size.

(7) The agreement between experimental systems and the isotropic strain-effect-free binary-alloy simulations is not yet satisfactory. The actual form factor seems to differ from system to system. Low molecular weight fluids and polymeric fluids appear to match very well with our binary-fluid simulations. This implies that no truly polymer effect on spinodal decomposition has been observed experimentally in critical and near-critical quench. We believe we do not need any special model to explain the various preasymptotic and asymptotic phenomena observed in polymer systems. Choosing appropriate parameters in the ordinary fluid model with or without the modification of the kinetic coefficient [see (16)] explains most observed phenomena even away from criticality.

(8) More technically, we have demonstrated that the cell-dynamical scheme modeling of spinodal decomposition at the mesoscopic level is very effective and reliable. Notice that our 192^3 implies far bigger systems than 192^3 lattice Monte Carlo or lattice-gas systems, because, e.g., each cell corresponds to at least a 4^3 lattice for the Monte Carlo method [2]. The relation to the conventional partial differential equation approach was discussed, and the concept of qualitative accuracy was advocated. We believe that the true reason for the qualitative accuracy is a kind of renormalization-group structure behind spinodal decomposition, but so far we have not been able to exploit this analytically.

(9) We have demonstrated that the spherically averaged form factor is essentially a self-averaging quantity, so that it is more advantageous to study a few very large systems than numerous (and inevitably) small systems, unless one wishes to accurately study the finite-size effect.

(10) We have pointed out that the conventional methods for computing the form factors and the pattern length scales are not optimal, and in some cases grossly misleading especially for binary fluids. Better schemes are proposed.

(11) Finally, we must point out that to check the asymptoticity, Tomita's sum rule is very useful, so that any conscientious computational work should give the Porod plot or the plot of $r^2G(r)$.

(12) Accurate binary-alloy experimental data which can give reliable Porod's plots is desirable.

(13) More accurate binary-fluid spinodal decomposition with low molecular weight compounds is desirable.

We feel that to get the true asymptotic results for binary fluids, we will need a 512^3-sized system. Only one sample is needed, so this will be feasible in the near future.

ACKNOWLEDGMENTS

The authors gratefully acknowledge the continuous encouragements of Myron Salamon and Jim Wolfe throughout the course of the study since the insemination of the CDS scheme. Y.O. acknowledges useful correspondence with Takeji Hashimoto, Takao Ohta, Hiroyuki Tomita, and Chuck Yeung. The preliminary stage of the binary-alloy study was, in part, supported by the National Science Foundation Grant No. NSF-DMR-89-20538 administered by the University of Illinois Materials Research Laboratory. The main part of the project was, in part, supported by the National Science Foundation Grant No. NSF-DMR-90-15791 and National Center for Supercomputing Applications Grant No. DMR-89-0104N. S.A. received support from the Beckman Institute.

APPENDIX. COMPARISON OF CDS BINARY FLUID MODELS

To assess the effect of our coarse-grained dynamics, we did several comparative experiments, all starting from identical initial conditions, and we varied the dynamics. Each system was 64^3 in size with the tanh map, $D=0.7$, $A=1.3$, $\nu=1.0$, and $M=1.0$. Four schemes are compared: the additive scheme without skipping of the velocity update (anv); the split step scheme without skipping of the velocity updata (snv); the additive scheme with the velocity update skipping with a maximum skip of 10 iterations (av); and the split step scheme with velocity update skipping (sv). We computed the scattering function at various t_{CDS} for each run, and compared $\langle k \rangle$, $S(k)$, $k^4S(k)$, and finally the volume-normalized functional distance between the different runs for patterns generated at the same t_{CDS}.

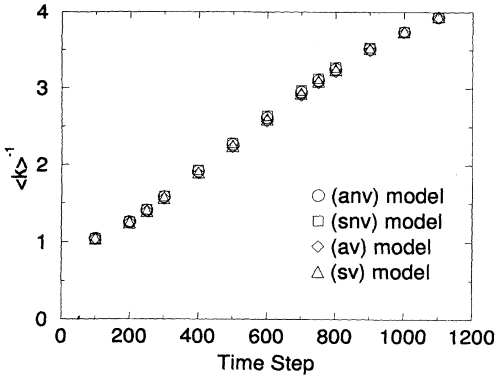

FIG. 66. Plot of $\langle k \rangle$ for different hydrodynamic simulation models described in the text. The systems studied used the tanh map with $A=1.3$, $D=0.7$, and $\eta=1.0$, and were of size 64^3.

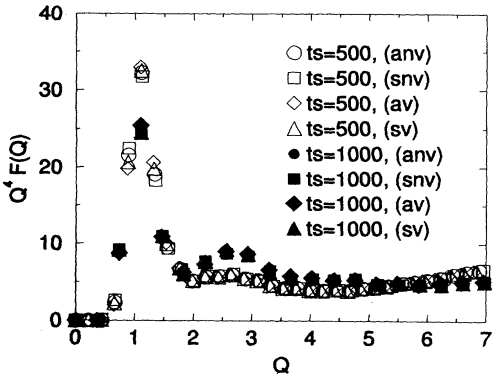

FIG. 68. Scaled Porod's plot $Q^4F(Q)$ vs Q for different hydrodynamic simulation models described in the text. Two different time steps are sampled, one at $t_{CDS}=500$ and the other at $t_{CDS}=1000$. Note that subtle features of Porod's plot are indistinguishable between models.

In Fig. 66 we have plotted $\langle k \rangle^{-1}$ versus t_{CDS} for the four schemes. There is little change in the growth law among them. The most appreciable change is at about $t_{CDS}=700$, where there is about a 5% difference between $\langle k \rangle^{-1}$ of (snv) and (av), where (snv) is the most advanced in growth. The other two schemes lay between these points. The $\langle k \rangle^{-1}$ actually appear to coalesce above $t_{CDS}=1000$, where finite-size effects become effective and slow down the increase of $\langle k \rangle$ in general.

In Fig. 67 we see that the various values of $S(k)$ taken for each scheme at two different times outline essentially the same function. The slight separation of the data points at a given time for the different models is consistent with the above shift of the $\langle k \rangle$ for the different models. Note that (av) again lags the most, and (snv) is the most advanced, with the other schemes in between. A closer inspection of the high-k region of $S(k)$ in Fig. 68 via Porod's plot, $S(k)k^4$ versus k, shows that the very sensitive detail of the small-scale structure is numerically indistinguishable. Even the changes over time appear to be the same.

The l^2 distance of the patterns between all pairs of models over time is plotted in Fig. 69. Most of the pairs compared follow the same distance change over time. The most significant difference is found between the (av) and (snv), consistent with their difference in $\langle k \rangle$. A quick calculation shows that the difference in $\langle k \rangle$ accounts for the distance. First assume that the patterns are nearly the same, except that one model is slightly more coarsened. Call one model A and the other B. $\langle k \rangle^{-1} \propto l$, where l is roughly the size of domains. The bulk regions of A and B largely overlap, and contribute nothing to the distance. At the interfaces, there is a slight mismatch due to the difference in coarsening. At worst, in a cell of a region which is mismatched, the distance is increased by $2/V$. The number of mismatched cells is roughly $|1-(\langle k \rangle_A/\langle k \rangle_B)^3|V$. Hence the upper bound on the deviation is roughly $2|1-(\langle k \rangle_A/\langle k \rangle_B)^3|$. We noted above that the worst deviation is about 5% in

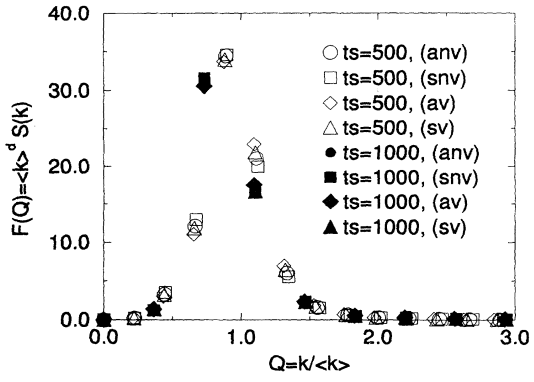

FIG. 67. Plot of $F(Q)$ vs Q for different hydrodynamic simulation models described in the text. Two different time steps are sampled, one at $t_{CDS}=500$ and the other at $t_{CDS}=1000$.

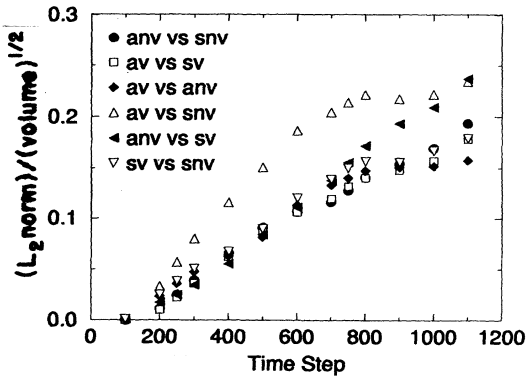

FIG. 69. Plot of the l_2 distance between different hydrodynamic model simulations, all started from the same random initial conditions.

$\langle k \rangle$, so that the distance should be roughly 0.28, which is close to what we observe for the worst matching models.

In conclusion, the different models lead to patterns which are essentially the same as analyzed by the scattering form factor. The difference in the models is a slight shift in the coarsening rates from model to model, and this shift in rate accounts for the functional distance between the patterns generated by the different models at corresponding t_{CDS}.

*Present address: Department of Physics and Astronomy, University of Pittsburgh, Pittsburgh, PA 15260.

[1] J. W. Cahn and J. I. Hilliard, J. Chem. Phys. **28**, 258 (1958).
[2] Y. Oono and A. Shinozaki, Forma **4**, 75 (1989).
[3] Y. Oono, IEICE Trans. E **74**, 1379 (1991).
[4] K. Binder and D. Stauffer, Phys. Rev. Lett. **33**, 1006 (1974); Adv. Phys. **25**, 343 (1976).
[5] H. Furukawa, Phys. Lett. A **62**, 377 (1977); Prog. Theor. Phys. **59**, 1072 (1978).
[6] A. Coniglio and M. Zannetti, Europhys. Lett. **10**, 575 (1989).
[7] A. Coniglio, Y. Oono, A. Shinozaki, and M. Zannetti, Europhys. Lett. **18**, 59 (1992).
[8] E. D. Siggia, Phys. Rev. A **20**, 595 (1979).
[9] K. Kawasaki and T. Ohta, Physica A **118**, 175 (1983).
[10] Y. Oono and M. Bahiana, Phys. Rev. Lett. **61**, 1109 (1988).
[11] M. Grant, Phys. Rev. Lett. **62**, 1065 (1989).
[12] S. Spooner, in *Kinetics of Aggregation and Gelation,* edited by F. Family and D. P. Landau (North-Holland, Amsterdam, 1984).
[13] B. D. Gaulin, S. Spooner, and Y. Morii, Phys. Rev. Lett. **59**, 668 (1987).
[14] S. Katano and M. Iizumi, Phys. Rev. Lett. **52**, 835 (1984).
[15] M. Hennion, D. Ronzaud, and P. Guyot, Acta Metall. **30**, 599 (1982).
[16] A. F. Craievich, J. M. Sanchez, and C. E. Williams, Phys. Rev. B **34**, 2762 (1986).
[17] N.-C. Wong and C. M. Knobler, J. Chem. Phys. **69**, 725 (1978).
[18] Y. C. Chou and W. I. Goldburg, Phys. Rev. A **23**, 858 (1981).
[19] T. Hashimoto, M. Itakura, and H. Hasegawa, J. Chem. Phys. **85**, 6118 (1986); T. Izumitani, M. Takenaka, and T. Hashimoto, *ibid.* **92**, 3213 (1990); M. Takenaka, T. Izumitani, and T. Hashimoto, *ibid.* **2**, 4566 (1990).
[20] F. S. Bates and P. Wiltzius, J. Chem. Phys. **91**, 3258 (1989).
[21] J. G. Amar, F. E. Sullivan, and R. D. Mountain, Phys. Rev. B **37**, 196 (1988).
[22] C. Roland and M. Grant, Phys. Rev. B **39**, 11 971 (1989).
[23] J. Marro, J. L. Lebowtiz, and M. H. Kalos, Phys. Rev. Lett. **43**, 282 (1979); J. L. Lebowitz, J. Marro, and M. H. Kalos, Acta. Metall. **30**, 297 (1982).
[24] J. Viñals and D. Jasnow, Phys. Rev. B **37**, 9582 (1988).
[25] W.-J. Ma, A. Maritan, J. R. Banavar, and J. Koplik, Phys. Rev. A **45**, R5347 (1992).
[26] T. M. Rogers, K. R. Elder, and R. Desai, Phys. Rev. B **37**, 9638 (1988).
[27] A. Chakrabarti, R. Toral, and J. D. Gunton, Phys. Rev. B **39**, 4386 (1989).
[28] Y. Oono and S. Puri, Phys. Rev. Lett. **58**, 836 (1987); Phys. Rev. A **38**, 434 (1988); S. Puri and Y. Oono, *ibid.* **38**, 1542 (1988).
[29] A. Chakrabarti and J. D. Gunton, Phys. Rev. B **37**, 3798 (1988).
[30] A. Shinozaki and Y. Oono, Phys. Rev. Lett. **66**, 173 (1991).
[31] A. Shinozaki and Y. Oono, Phys. Rev. A **45**, R2161 (1992).
[32] T. Koga and K. Kawasaki, Phys. Rev. A **44**, R817 (1991).
[33] C. Yeung, Phys. Rev. Lett. **61**, 1135 (1988).
[34] H. Furukawa, J. Phys. Soc. Jpn. **58**, 216 (1989); Phys. Rev. B **40**, 2341 (1989).
[35] H. Tomita, in *Formation, Dynamics and Statistics of Patterns,* edited by K. Kawasaki *et al.* (World Scientific, Singapore, 1990), Vol. 1.
[36] A. J. Bray and S. Puri, Phys. Rev. Lett. **67**, 2670 (1991).
[37] H. Toyoki, Phys. Rev. B **45**, 1965 (1992).
[38] D. Jasnow and R. K. P. Zia, Phys. Rev. A **36**, 2243 (1987).
[39] A. Shinozaki and Y. Oono, Phys. Rev. E **47**, 804 (1993).
[40] A. Shinozaki, Phys. Rev. E **48**, 1984 (1993).
[41] H. Furukawa, Adv. Phys. **34**, 703 (1985).
[42] G. Porod, in *Small Angle X-ray Scattering,* edited by O. Glatter and L. Kratky (Academic, New York, 1983).
[43] H. Tomita, Prog. Theor. Phys. **75**, 482 (1986).
[44] H. Tomita, Prog. Theor. Phys. **85**, 47 (1991).
[45] S. Puri and Y. Oono, J. Phys. A **21**, L755 (1988).
[46] K. Kitahara, Y. Oono, and D. Jasnow, Mod. Phys. Lett. B **2**, 765 (1988).
[47] J. S. Langer, M. Bar-On, and H. D. Miller, Phys. Rev. A **11**, 1417 (1975).
[48] K. Kitahara and M. Imada, Prog. Theor. Phys. Supp. **64**, 65 (1978).
[49] C. Yeung, Ph.D. thesis, University of Illinois, Urbana–Champaign, 1988.
[50] K. Kawasaki, Prog. Theor. Phys. **57**, 826 (1977).
[51] M. Bahiana and Y. Oono, Phys. Rev. A **41**, 6763 (1990).
[52] M. Takenaka, T. Izumitani, and T. Hashimoto, J. Chem. Phys. **97**, 6855 (1992).
[53] S. Nojima, K. Tsutsumi, and T. Nose, Polym. J. **14**, 225 (1982); M. Takahashi, H. Horiuchi, S. Kinoshita, Y. Ohyama, and T. Nose, J. Phys. Soc. Jpn. **55**, 2687 (1986).
[54] M. Okada and C. C. Han, J. Chem. Phys. **85**, 5317 (1986).
[55] P. G. de Gennes, J. Chem. Phys. **72**, 4756 (1980).
[56] P. Pincus, J. Chem. Phys. **75**, 1996 (1981).
[57] K. Binder, J. Chem. Phys. **79**, 6387 (1983).
[58] T. Hashimoto (private communication).
[59] T. Hashimoto, T. Izumitani, and N. Shimizu, J. Chem. Phys. **85**, 6773 (1987).
[60] T. Hashimoto, T. Takenaka, and T. Izumitani, J. Chem. Phys. **97**, 679 (1992).
[61] A. Milchev, K. Binder, and D. W. Heermann, Z. Phys. B **63**, 521 (1986).
[62] Y. Oono and S. Puri, Mod. Phys. Lett. B **2**, 861 (1988).
[63] C. Yeung (private communication) pointed out that in the infinite volume limit $\psi(k)$ is Gaussian, so long as the correlation volume is finite.
[64] H. E. Stanley, D. Stauffer, J. Kertèsz, and H. Herrmann, Phys. Rev. Lett. **59**, 2326 (1987).
[65] This implies that the Reynolds number Re is proportional to t, so that eventually our Stokes approximation will fail.

In our simulation the velocity v is at most one hundredth of the lattice spacing ΔL per one time step Δt or $v \sim \Delta L/100\Delta t$, the kinematic viscosity is $\eta \sim \Delta t$, and the pattern size l is at most $20\Delta L$. Hence, $\mathrm{Re} \sim 0.2(\Delta L/\Delta t)^2$. Yeung pointed out that recently Furukawa has also discussed the inertial effect.

[66] H. Toyoki, Mod. Phys. Lett. B (to be published).

[67] P. Fratzl and J. L. Lebowitz, Acta Metall. **37**, 3245 (1989).

[68] M. K. Miller *et al.*, in *Kinetics of Aggregation and Gelation,* edited by F. Family and D. P. Landau (North-Holland, Amsterdam, 1984).

[69] T. Ohta and H. Nozaki, in *Space-Time Organization in Macromolecular Fluids,* edited by F. Tanaka, M. Doi, and T. Ohta, Springer Series in Chemical Physics Vol. 51 (Springer-Verlag, Berlin, 1989).

[70] G. Mazenko, Phys. Rev. B **43**, 5747 (1991).

[71] Y. Oono (unpublished); C. Yeung, Y. Oono, and A. Shinozaki (unpublished).

[72] M. Takenaka and T. Hashimoto, J. Chem. Phys. **96**, 6177 (1992).

[73] D. Roux, J. Phys. (Paris) **47**, 733 (1986).

[74] D. A. Huse, Phys. Rev. B **34**, 7845 (1986).

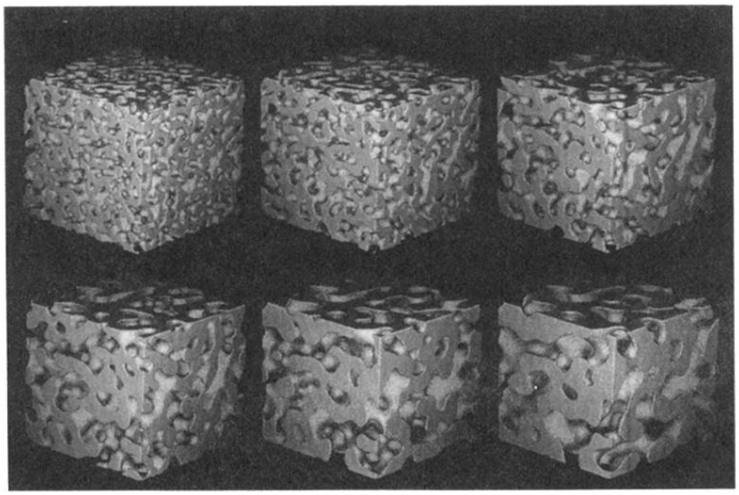

FIG. 16. $\psi=0$ isosurfaces of three-dimensional binary-alloy spinodal decomposition at critical quench. Parameters are $M_{\mathrm{CDS}}=1$, $D_{\mathrm{CDS}}=0.7$, and $A=1.15$ for the tanh map described in text. System size is 192^3. The images are a 128^3 subset of the entire sample. From top left to right, images are of $t_{\mathrm{CDS}}=1000$, 2000, and 4000 data, and, from bottom left to right, of $t_{\mathrm{CDS}}=7000$, 12 000, and 20 000 data.

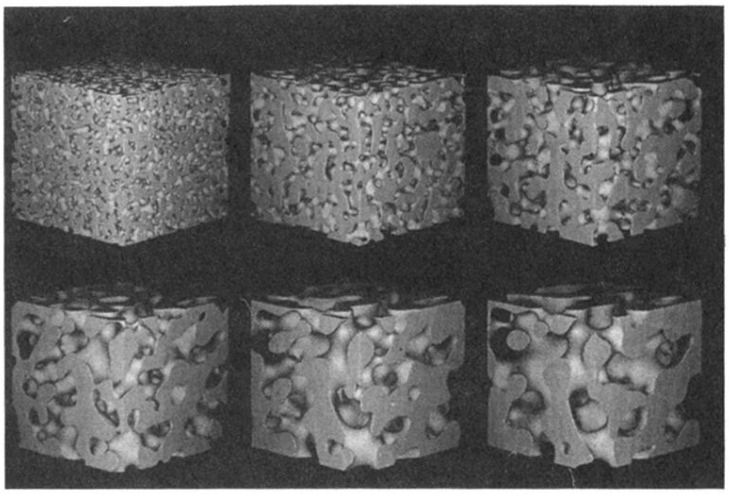

FIG. 32. $\psi=0$ isosurfaces of three-dimensional incompressible binary-fluid spinodal decomposition at critical quench. $\eta=1$, $M_{\mathrm{CDS}}=1$, and $D_{\mathrm{CDS}}=0.7$, using the tanh map described in the text with $A=1.3$. System size is 192^3. The entire 192^3 sample is exhibited. From top left to right, images are of $t_{\mathrm{CDS}}=500$, 1000, and 1500 data, and, from bottom left to right, of $t_{\mathrm{CDS}}=2000$, 2500, and 3000 data.

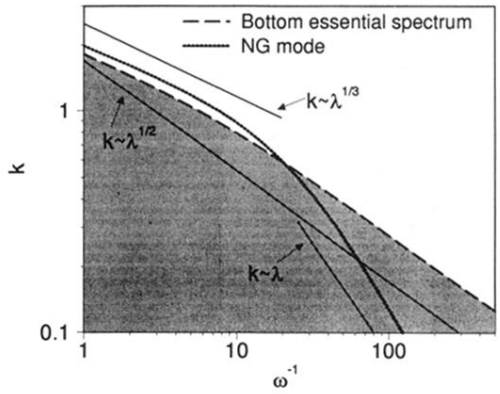

FIG. 62. Schematic description of the dispersion relation around the kink solution for the binary fluid with $\eta=1$. Plot of k vs ω^{-1} for $\eta=1$. The Nambu-Goldstone (NG) mode computed is represented by the dotted line. The dashed line is the bottom of the essential spectrum as estimated from the binary-alloy model. The gray area is the essential spectrum. Note the various power-law behaviors of the different branches in different regimes.